AFRL-AFOSR-UK-TR-2021-0011

DLR AS-HYP Transition Experiments on BOLT-Modell in H2K

Thiele, Thomas
DEUTSCHES ZENTRUM FUR LUFT- UND RAUMFAHRT E.V.
LINDER HOHE
KOLN, NORDRHEIN-WESTFALEN, 51147
DEU

06/21/2021
Final Technical Report

Air Force Research Laboratory
Air Force Office of Scientific Research
European Office of Aerospace Research and Development
Unit 4515 Box 14, APO AE 09421

REPORT DOCUMENTATION PAGE

Form Approved
OMB No. 0704-0188

1. REPORT DATE *(DD-MM-YYYY)*	**2. REPORT TYPE**	**3. DATES COVERED** *(From - To)*
21-06-2021	Final	15 Jul 2019 - 14 Jan 2021

4. TITLE AND SUBTITLE
DLR AS-HYP Transition Experiments on BOLT-Modell in H2K

5a. CONTRACT NUMBER

5b. GRANT NUMBER
FA9550-19-1-7028

5c. PROGRAM ELEMENT NUMBER

6. AUTHOR(S)
Thomas Thiele

5d. PROJECT NUMBER

5e. TASK NUMBER

5f. WORK UNIT NUMBER

7. PERFORMING ORGANIZATION NAME(S) AND ADDRESS(ES)
DEUTSCHES ZENTRUM FUR LUFT- UND RAUMFAHRT E.V.
LINDER HOHE
KOLN, NORDRHEIN-WESTFALEN 51147
DEU

8. PERFORMING ORGANIZATION REPORT NUMBER

9. SPONSORING/MONITORING AGENCY NAME(S) AND ADDRESS(ES)
EOARD
UNIT 4515
APO AE 09421-4515

10. SPONSOR/MONITOR'S ACRONYM(S)
AFRL/AFOSR IOE

11. SPONSOR/MONITOR'S REPORT NUMBER(S)
AFRL-AFOSR-UK-TR-2021-0011

12. DISTRIBUTION/AVAILABILITY STATEMENT
A Distribution Unlimited: PB Public Release

13. SUPPLEMENTARY NOTES

14. ABSTRACT
Within this report the experiments performed with the BOLT geometry in H2K at DLR are described. The acquired data are analysed in detail. Still to be done is the mapping of the IR data onto 3D surfaces and the computation of heat fluxes from the measured surface temperatures. Nevertheless the influence of Mach number, Reynolds number, angle of attack and yaw angle could be documented. Several interesting features including evidence for second (Mach) modes could be detected. It is planned to publish the findings in a journal paper.

15. SUBJECT TERMS

16. SECURITY CLASSIFICATION OF:			**17. LIMITATION OF ABSTRACT**	**18. NUMBER OF PAGES**	**19a. NAME OF RESPONSIBLE PERSON**
a. REPORT	**b. ABSTRACT**	**c. THIS PAGE**			DOUGLAS SMITH
U	U	U	SAR	46	**19b. TELEPHONE NUMBER** *(Include area code)* 314 235 6013

Final Report

Transition Experiments on BOLT-Model in H2K

Grant: FA9550-19-1-7028

Sebastian Willems, Thomas Thiele, Ali Gülhan

DLR German Aerospace Center
Institute of Aerodynamics and Flow Technology
Supersonic and Hypersonic Technologies Department
Köln

DLR Deutsches Zentrum für Luft- und Raumfahrt
German Aerospace Center

DLR German Aerospace Center
Institute of Aerodynamics and Flow Technology
Supersonic and Hypersonic Technologies Department
Prof. Dr. Ali Gülhan
Linder Höhe
51447 Köln
Germany
Tel: +49 2203 601-2363
Fax: +49 2203 601-2085
Web: http://www.dlr.de/as/en

Dr.-Ing. Sebastian Willems
Tel: +49 2203 601-2195
Fax: +49 2203 601-2085
Mail: sebastian.willems@dlr.de

Document Identification:

Title	Transition Experiments on BOLT-Model in H2K
Subject	Final Report
Author(s)	Sebastian Willems, Thomas Thiele, Ali Gülhan
Filename	Report.tex
Last saved on	June 12, 2021

Contents

List of Figures

List of Tables

Nomenclature

Abbreviations

AFOSR	Air Force Office of Scientific Research
APL	Johns Hopkins Applied Physics Laboratory
BAM6QT	Boeing/AFOSR Mach 6 Quiet Tunnel
BOLT	Boundary Layer Transition flight experiment (see section 1.2)
DLR	German Aerospace Center
GE	General Electric Company
H2K	hypersonic wind tunnel Cologne (see section 2.1)
HIFiRE	Hypersonic International Flight Research Experimentation program
IR	infrared
KPT	Kulite® pressure transducers
MTB	MTB Sensor-Technik GmbH
NI	National Instruments™
PCB	PCB® Piezotronics
PEEK	polyether ether ketone (a high temperature plastic)
PSI	Pressure Systems, Inc.
TCK	thermocouple type K
Baratron	MKS Baratron®

Latin Symbols

Ma	Mach number
p	(static) pressure
Re	Reynolds number
Re_{u}	unit Reynolds number
T	(static) temperature
v	flow velocity
x	x-coordinate
y	y-coordinate
z	z-coordinate

Greek Symbols

α	angle of attack
β	yaw angle

Subscripts

0	reservoir conditions
∞	free stream conditions

1 Introduction

At hypersonic speeds the transition from a laminar to a turbulent boundary layer is attended by an increase in the drag by a factor of more than two and an increase in the heat flux by a factor of more than four. Therefore, big areas of laminar flow are desirable to increase the performance of a propelled vehicle and to reduce the weight of the necessary thermal protection systems of a propelled or re-entry vehicle. On the other hand, turbulent boundary layers have a lower tendency to separate and are preferred in regions of large pressure gradients as intakes or control surfaces. Hence, the correct prediction of the transition is essential for the design of future hypersonic vehicles and their thermal protection systems.

1.1 Existing research

The transition from laminar to turbulent boundary layers in hypersonic flows is influenced by several factors as Mach number, Reynolds number, surface temperature, chemical reactions, high enthalpy effects, surface shape, angle of attack, roughness, free stream disturbances and so on. To reduce complexity a lot of research into hypersonic boundary layer transition was made on generic geometries with two dimensional or pseudo two dimensional flows as flat plates or axially symmetric configurations (especially on circular straight 7° half angle cones as used for the HIFiRE-1). As the first mode (Tollmien-Schlichting waves) is damped by cold surfaces, the second mode (Mack mode) becomes dominant in case of natural transition. The formation and amplification of these acoustic waves trapped in the boundary layer have been the topic of several research projects.

Transition in three dimensional flow fields has been investigated recently usually on convex surfaces - either on circular cones with an angle of attack (especially for HIFiRE-1) or on elliptic cones (especially for HIFiRE-5a and HIFiRE-5b). Other investigations of transition with three dimensional flow fields deal with flow structures induced by disturbing elements.

1.2 Boundary Layer Transition flight experiment (BOLT)

Boundary Layer Transition flight experiment (BOLT) is a project financed by the Air Force Office of Scientific Research (AFOSR) and lead by the Johns Hopkins Applied Physics Laboratory (APL). The aim is the investigation of the transition process on a more complex geometry with concave surfaces and swept leading edges at a Mach number between 5 and 7. It is expected, that cross flow instabilities influence the transition process significantly. In addition the effect of surface roughness is tested on the identical upper and lower surface [5].

Existing ground test data performed in the Boeing/AFOSR Mach 6 Quiet Tunnel (BAM6QT) at Purdue University suggests that transition is caused by a combination of second mode waves (Mack mode) and stationary crossflow vortices or traveling crossflow waves [1].

1.3 Investigation within this project

The goals of the investigations at German Aerospace Center (DLR) are on the one hand to reproduce existing investigations in another test section and another team and on the other hand to expand the scope of the investigated conditions. The latter one are namely investigating different Mach numbers, different angles of attack and yaw angles. As the flight configuration was already fixed, another goal was to perform experiments with an instrumentation close to the flight model.

2 Experimental setup

2.1 Hypersonic wind tunnel Cologne (H2K)

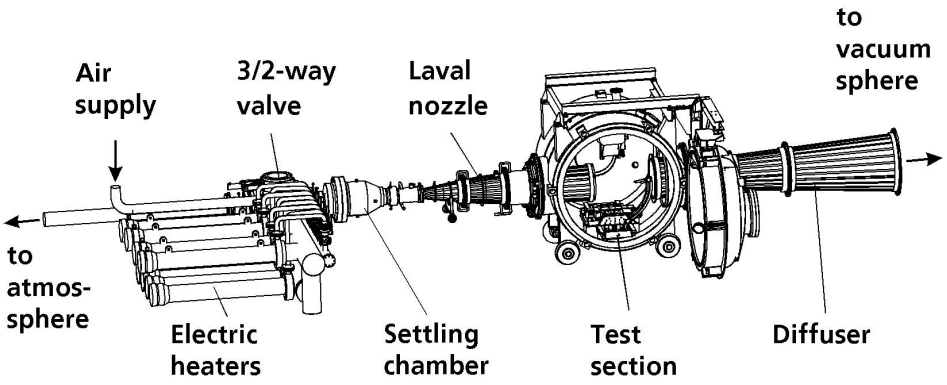

Figure 2.1: Sketch of H2K

The experiments were performed in the hypersonic wind tunnel Cologne (H2K) [4]. It is a blow-down wind tunnel with a free jet test section and a test time of 30 s (figure 2.1). Figure 2.3b shows the test section with the model installed. For the experiments contoured nozzles with an exit diameter of 600 mm were used. The test gas is dry air and heated with electrical resistance heaters.

2.2 Model

The model used for the experiments (figure 2.2) is a 1:2 scale of the BOLT geometry. The first design goal was to allow an instrumentation similar to the BOLT flight model. The second goal was to use as few parts as possible, to reduce the number of intersections and hence possible sources of disturbances and to put the intersections where interferences with the measurements are unlikely. The third goal was to use polyether ether ketone (PEEK) – a low conductive high temperature plastic – wherever possible to allow infrared (IR) thermography of the surface. Therefore the model consists of just three main parts: a steel nose, a PEEK main body and a PEEK lid. Most of the sensors are integrated in the lid, that forms the top side of the model. The intersection to the main body is just

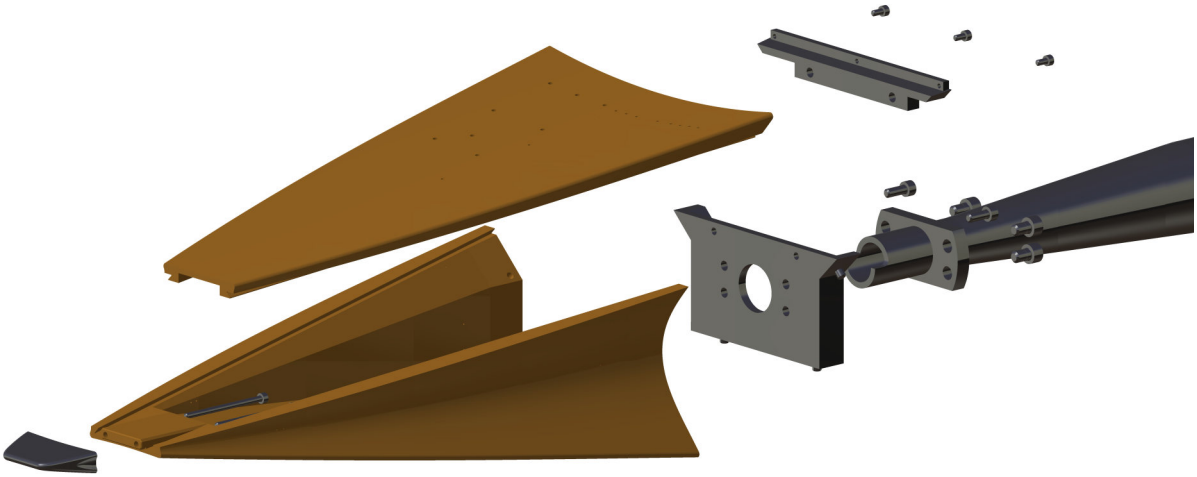

Figure 2.2: Exploded view of the wind tunnel model

below the upper shoulder on the sides. A steel flange forms the back of the model, with which it is mounted onto a stiff sting to avoid model vibrations during the tests. As the model is attached to the standard H2K support arm, different angles of attack and yaw angles can be set easily. Figures 2.3a and 2.3b show the BOLT model in H2K. The midpoint of the leading edge of the model is the origin of the coordinate system used in this report. The x-axis points in the flow direction, the y-axis points upwards to the top side of the model and the z-axis is parallel to the leading edge.

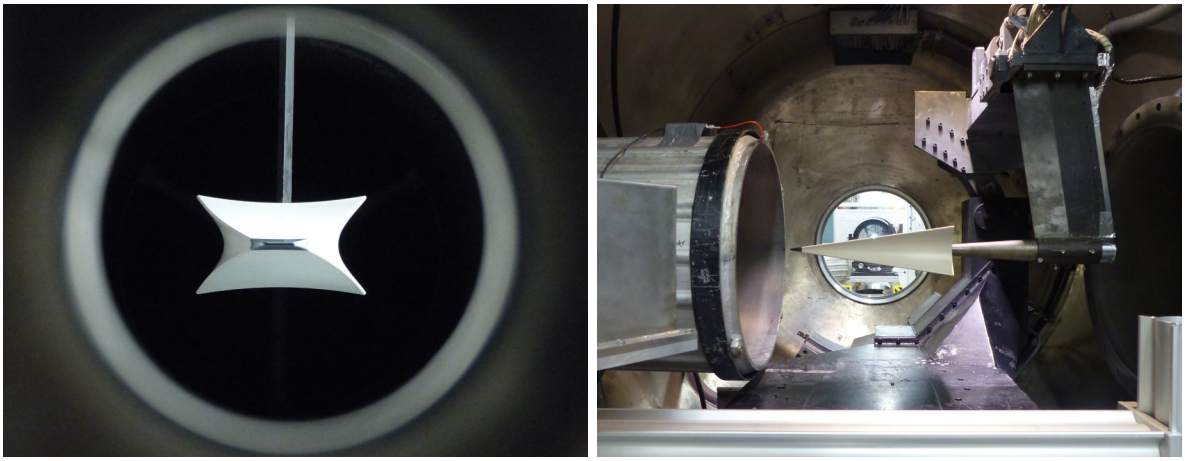

(a) front view **(b)** side view

Figure 2.3: BOLT model in H2K

2.3 Instrumentation

The sensor instrumentation is based on the instrumentation of the flight model. There are 8 PCB® Piezotronics (PCB) 132A31 sensors for high speed pressure measurements at the same locations as in flight. They are connected to PCB 482C05 signal conditioners. Their output signals are processed with ADLINK PXI-9816D/512 digitizers at 5 MHz sampling frequency. 10 Kulite® pressure transducers XCE-080-0.35BarA absolute pressure sensors duplicate the last row and positions in the symmetry plane of mid-speed pressure sensors of the flight model. They are connected to a National Instruments™ (NI) PXIe-4331 bridge module and sampled at 100 kHz. The static pressure measurements are performed with 5 psi Initium pressure scanners from Pressure Systems, Inc. (PSI) at 50 Hz sampling rate. Figure 2.4 sketches the sensor positions on the model surface and the senor numbering. For the exact sensor positions see appendix A.1.

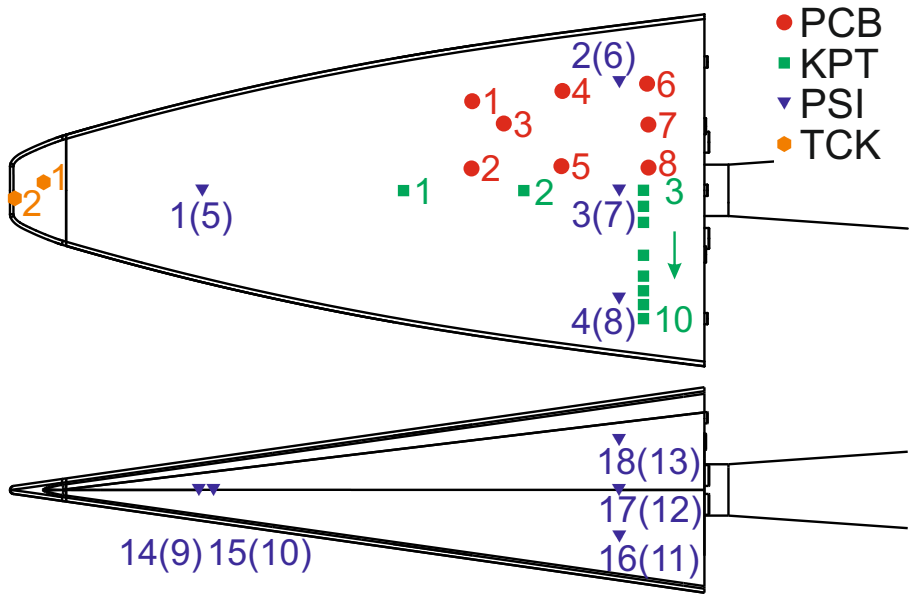

Figure 2.4: Positions and numbering of the sensors. Numbers in brackets refer to the counterparts on the opposing surfaces.

The temperature distribution of the top side of the model was recorded with an IRCAM VELOX 1310k SM with a resolution of 1280x1024 pixel and one side was monitored with an Infratec ImageIR 8300 with 1280x1024 pixel pixel resolution. Both cameras were sampled at 100 Hz. Schlieren images were taken with a Nikon Z6 with 1280x1024 pixel resolution and $\frac{1}{3200}$ s exposure time. As the surface temperature of the metallic nose cannot be determined based on the IR measurements, there are two thermocouples

type K (TCK) class 1 from MTB Sensor-Technik GmbH (MTB) placed 3 mm and 21 mm from the leading edge inside the nose. They are sampled at 50 Hz with a NI PXIe-4353 temperature module.

The flow temperature in the settling chamber is also measured with a thermocouple type K class 1 from MTB sampled at 50 Hz with a NI PXIe-4353 temperature module. In the settling chamber the pitot pressure is measured with a General Electric Company (GE) UNIK 5000 pressure sensor. A zero correction of this sensor as well as the PSI and Kulite® pressure transducers are done before each run using a MKS Baratron® (Baratron) consisting of a 398HD pressure transducer and a 270B-4 signal conditioner as reference. The signals of the GE and Baratron sensors are digitized with a NI PXI-6289 multifunction module at 50 Hz sampling rate.

2.4 Test Matrix

Experiments were performed at three different Mach numbers, three unit Reynolds numbers a number of angle of attacks and yaw angles. The complete test matrix with nominal flow conditions is given in table 2.1. A detailed list of the performed tests with the measured flow conditions is given in appendix A.2.

Table 2.1: Test matrix for the H2K experiments

Flow conditions				Model configurations		
Ma_∞ [ ]	T_0 [K]	p_0 [kPa]	$Re_{u,\infty}$ $\left[\frac{1}{m}\right]$	α	β	$(\alpha;\beta)$
5.3	470	250	$3 \cdot 10^6$	0°	0°	-
5.3	470	500	$6 \cdot 10^6$	0°	0°	-
5.3	470	1 000	$12 \cdot 10^6$	0°	0°	-
6.0	500	373	$3 \cdot 10^6$	0°, ±2°, ±4°, 6°, ±8°	0°, ±2°, ±4°	(2°; 2°)
6.0	500	750	$6 \cdot 10^6$	0°	0°	-
6.0	500	1 500	$12 \cdot 10^6$	0°	0°	-
7.0	600	730	$3 \cdot 10^6$	0°, ±2°, ±4°, 8°	0°, ±2°, ±4°	-
7.0	600	1 460	$6 \cdot 10^6$	0°	0°	-
7.0	600	2 920	$12 \cdot 10^6$	0°	0°	-

3 Results

3.1 Static pressure measurements

3.1.1 Model alignment

The static pressure measurements are highly sensitive to the angle of attack α and yaw angle β. The other way round they can be used to determine the actual attitude quite well. The pressure differences between the pressure taps on the upper surface and their counterparts on the lower surface correlate linear to the angle of attack α and are not influenced by the yaw angle β. This is shown in figure 3.1, were points mark measured values and lines linear trends. The dotted black lines represents analytic values for a wedge with 6.875° half angle, which is the half angle of the BOLT geometry in the symmetry plane. They are computed with the equations for oblique shock waves and Prandtl–Meyer expansions respectively.

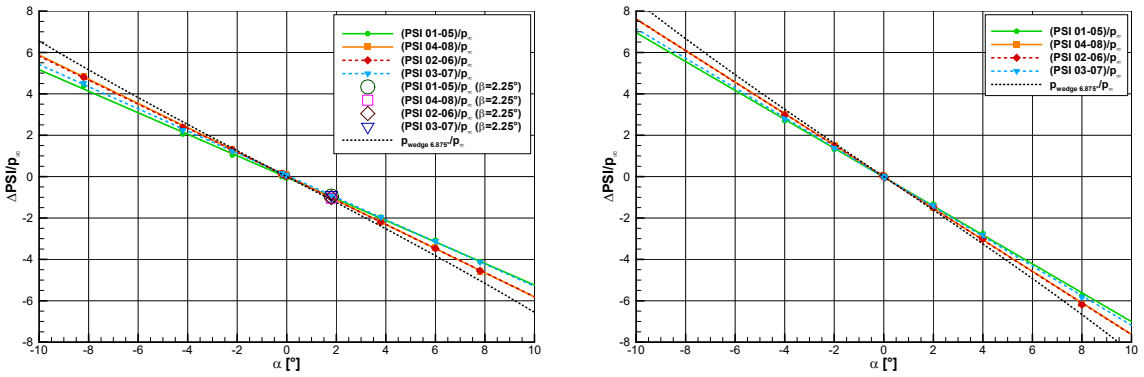

(a) $Ma_\infty = 6.0$ **(b)** $Ma_\infty = 7.0$

Figure 3.1: Differences of static pressure measurements between upper and lower surface with respect to angle of attack α normalized with the static pressure of the inflow p_∞

Analogue pressure differences between the pressure taps on the sides and their counterparts correlate linear to the yaw angle β and are not influenced by the angle of attack α. This is shown in figure 3.2. As the results are apparently reliable, they were used to

determine and correct the model alignment beginning with run 21. The post processing of the runs 1 to 20 showed that the values of α were 0.2° lower than planned and the values of β 0.25° higher than planned. To have at least one run with zero angle of attack and yaw angle some additional runs were performed at the end of the test campaign (runs 35 to 37). All specifications of α and β within this report including the table in appendix A.2 are corrected values.

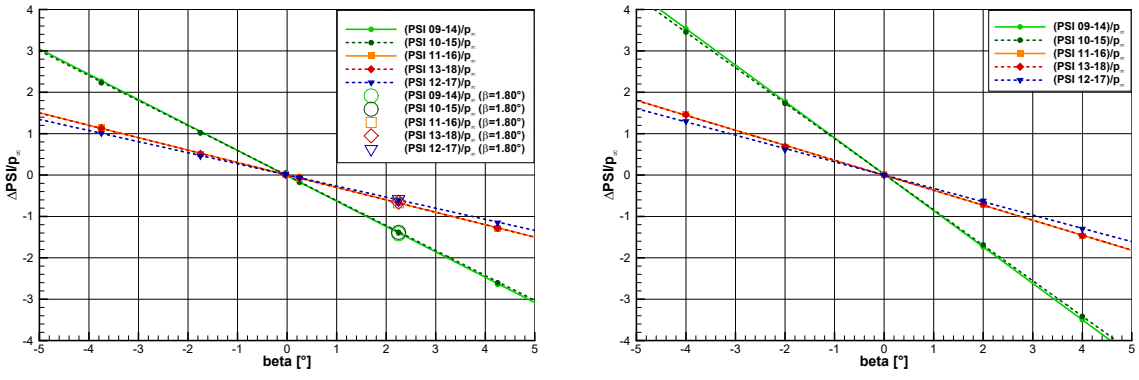

(a) $Ma_\infty = 6.0$ **(b)** $Ma_\infty = 7.0$

Figure 3.2: Differences of static pressure measurements between right and left side with respect to yaw angle β normalized with the static pressure of the inflow p_∞

3.1.2 Wall pressure

As the absolute wall pressures proved to be useful to normalize the dynamic pressure measurements as shown in section 3.2.2, they are plotted in figure 3.3 scaled with the normal pressure of the inflow p_∞. Here the pressures of the upper side are plotted against α and those of the lower side against $-\alpha$. Again points mark measured values, lines trends – here based on third order polynomials – and the dotted black lines analytic values for a wedge with 6.875° half angle.

3.2 Dynamic pressure measurements

3.2.1 Particle impacts

As the BOLT geometry is quite flat and there are no devices that deflect the flow towards the surface, it was expected during the design phase, that particle impacts are not a big

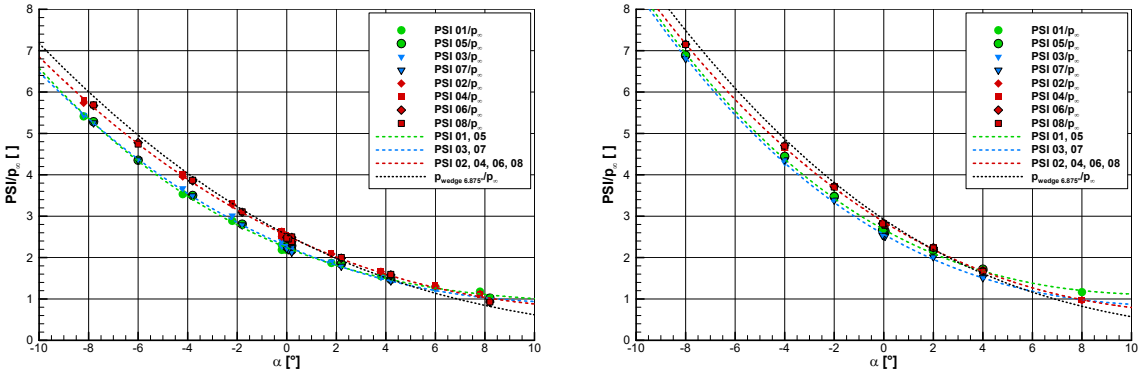

(a) $Ma_\infty = 6.0$ **(b)** $Ma_\infty = 7.0$

Figure 3.3: Static pressure measurements with respect to angle of attack α normalized with the static pressure of the inflow p_∞. Pressures from the lower side are plotted against $-\alpha$.

issue for these experiments. Therefore it seemed reasonable to use sensors with M-screens instead of B-screens to bridge the gap to the high-speed pressure measurements, as they have the better frequency response. Nevertheless the measurements show that occasionally particle impacts happened, as for example in the raw data of KPT01 during run 7 shown in figure 3.4a. It is obvious, that the average value is shifted by the impact at 13 s.

In figure 3.4b several computations of the power spectral density are plotted for this data set. The computed spectra before and after the impact are the same for frequencies above 200 Hz, but the spectrum for the complete data set is disturbed up to 3 kHz. Subtracting a running average does not solve this problem, but the subtraction of a running median does. The draw back of this strategy is the time consuming computation of a running median an the blurred spectra for frequencies below 200 Hz. Therefore an algorithm was implemented, that detects the impact based on the local standard deviation and excludes the affected blocks from the spectrum computation based on Welch's method. This procedure is more efficient and preserves the characteristic of the complete spectrum.

About half of the Kulite pressure transducers are heavily hit by a particle at least once during the test campaign, but it does not seem to have a permanent effect on the dynamic properties of the sensors, as the spectra at similar conditions do not change significantly. This is shown in figure 3.5a for KPT06, which is heavily hit by a particle during run 11. In contrast to that the dynamic properties of KPT03 for frequencies below 200 Hz change permanently after impacts during run 8 and run 11, as it can be seen in figure 3.5b. Nevertheless for the analysis within this report data are excluded

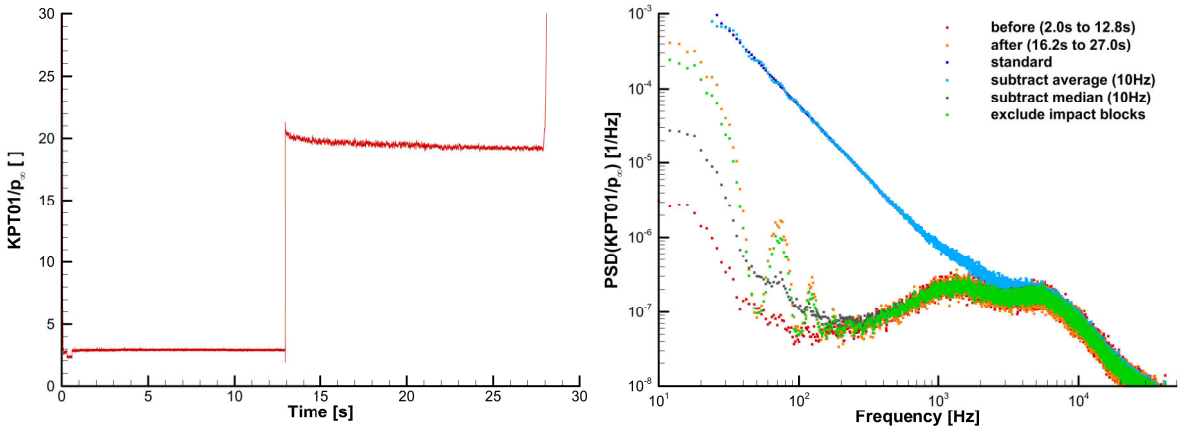

(a) Raw data **(b)** Power spectral density

Figure 3.4: Example of a particle impact. Here KPT03 during run 7.

that are affected by particle impacts. This is especially true for KPT03 for all runs after run 7.

3.2.2 Spectrum scaling

Usually dynamic pressures are scaled with the static pressure of the inflow p_∞ when computing power spectral densities, which allows a better comparison of measurements at different inflow conditions. But as the surface pressure also depends on the Mach number Ma and the angle of attack α, it was found, that the time averaged surface pressures are more suitable for the normalization of the dynamic pressures. Due to the shift of the mean value of the Kulite pressure transducers after a particle impact and the incapability of PCB sensors to measure static pressures, the measurements of the PSI scanners are used for the scaling. For the KPT the average of PSI3 and PSI4 is used and for the PCB the average of PSI2 and PSI3. Figures 3.6a, 3.6c and 3.6e show examples of spectra for various $Re_{\mathrm{u},\infty}$, Ma_∞ and α scaled with the static pressure of the inflow p_∞. In comparison figures 3.6b, 3.6d and 3.6f the same curves scaled with the surface pressures measured of the PSI sensors. As expected the comparison shows, that for the inflow conditions the change of the scaling does not make a difference, just the absolute values change. For the Mach number the effect is small, but the curves move a little bit closer together. For the angle of attack there is a significant effect, which could even influence the conclusion whether a curve is from a laminar or turbulent boundary layer.

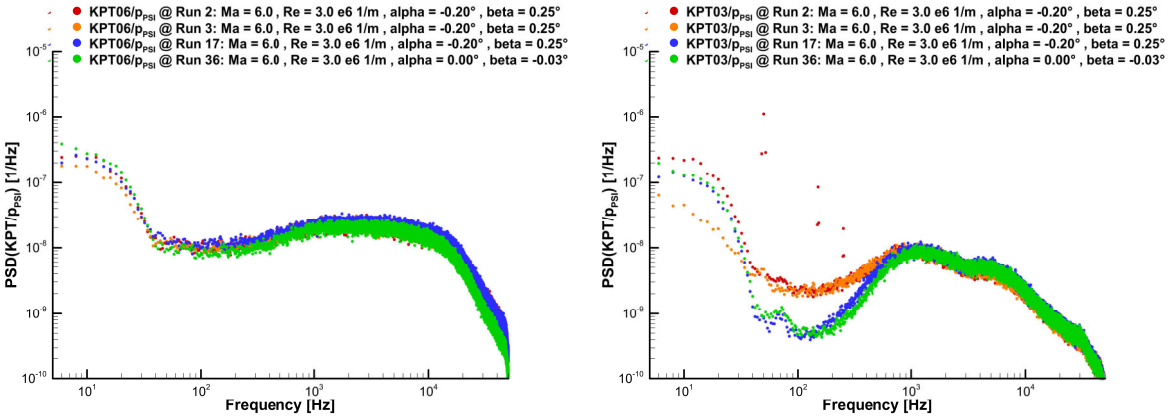

(a) KPT06 $x = 395.000\,\text{mm}$, $z = 40.500\,\text{mm}$ **(b)** KPT03 $x = 395.000\,\text{mm}$, $z = 0.000\,\text{mm}$

Figure 3.5: Repeatability of power spectral densities over the test campaign

3.2.3 Reynolds number and Mach number effect

Figures 3.7 to 3.9 show for Ma_∞ equal to 5.3, 6.0 and 7.0 and $Re_{\text{u},\infty}$ equal to $3 \cdot 10^6\,\frac{1}{\text{m}}$, $6 \cdot 10^6\,\frac{1}{\text{m}}$ and $12 \cdot 10^6\,\frac{1}{\text{m}}$ the power spectral densities of all Kulite pressure transducers on the left hand side and of all PCB on the right hand side. The analysis of the KPT spectra shows two interesting ranges, frequencies below and above 30 Hz. They seem to behave quite different and are therefore presumably connected to different flow features. The interesting range of the PCB sensors is from 40 kHz to 300 kHz, above and below there seems to be mostly noise. The fringe sensors PCB1, PCB4 and PCB6 show a transition process that includes something similar to a second (Mach) mode at frequencies between 100 kHz and 200 kHz. For some cases this can also be found in the spectra of the intermediate sensors PCB3 and PCB7. In contrast to that the central PCB close to the symmetry plane (PCB2, PCB5 and PCB8) do not reveal any interesting data, presumably as they are located underneath the central vortices predicted by Knutson *et al.* [2] and measured by Kostak and Bowersox [3].

Starting with figure 3.7a that shows measurements at $Ma_\infty = 5.3$ and $Re_{\text{u},\infty} = 3 \cdot 10^6\,\frac{1}{\text{m}}$ it can be seen that the spectra of KPT01 to KPT05 build one group and KPT06 to KPT10 another one. While the latter ones are almost identical, the former ones show increasing amplitudes for frequencies around 1 kHz. KPT01 and slightly KPT02 reveal a double peaks in the high frequency range. One around 1.4 kHz and one around 5.4 kHz. At frequencies lower than 30 Hz just KPT01 and KPT05 measure amplitudes lower than the others. Based on the following findings, first signs of second order (Mach) modes can be found in the spectra of PCB1, PCB3 and PCB4 at frequencies slightly below 200 kHz. PCB6 is presumably located in the turbulent boundary layer and PCB7 in the laminar boundary layer. PCB2, PCB5 and PCB8 show continuously quite low amplitudes but

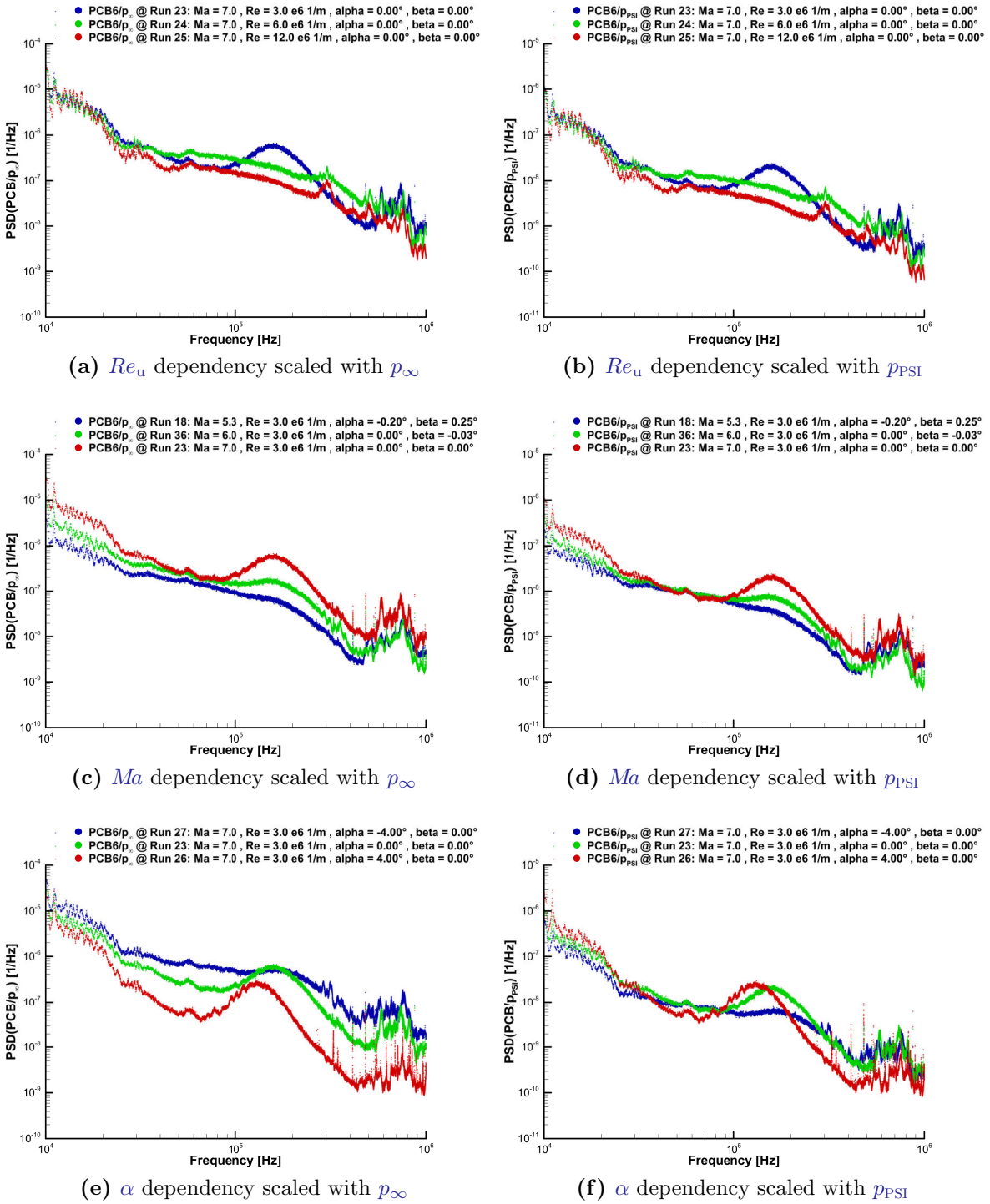

(a) Re_{u} dependency scaled with p_{∞}

(b) Re_{u} dependency scaled with p_{PSI}

(c) Ma dependency scaled with p_{∞}

(d) Ma dependency scaled with p_{PSI}

(e) α dependency scaled with p_{∞}

(f) α dependency scaled with p_{PSI}

Figure 3.6: Scaling of power spectral densities

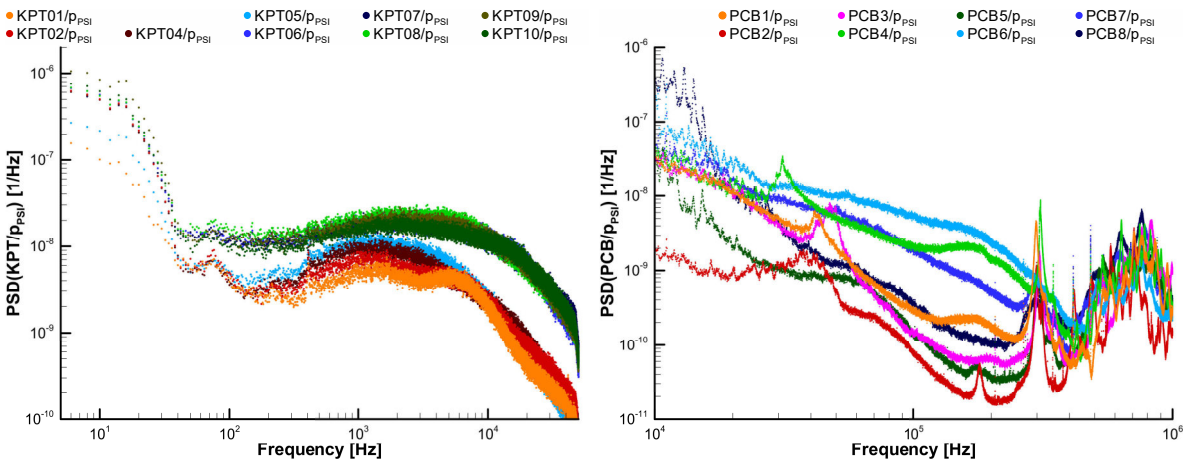

(a) run 18: $Ma_\infty = 5.276$, $Re_{\mathrm{u},\infty} = 3.059 \cdot 10^6 \, \frac{1}{\mathrm{m}}$, $\alpha = -0.20°$, $\beta = 0.25°$

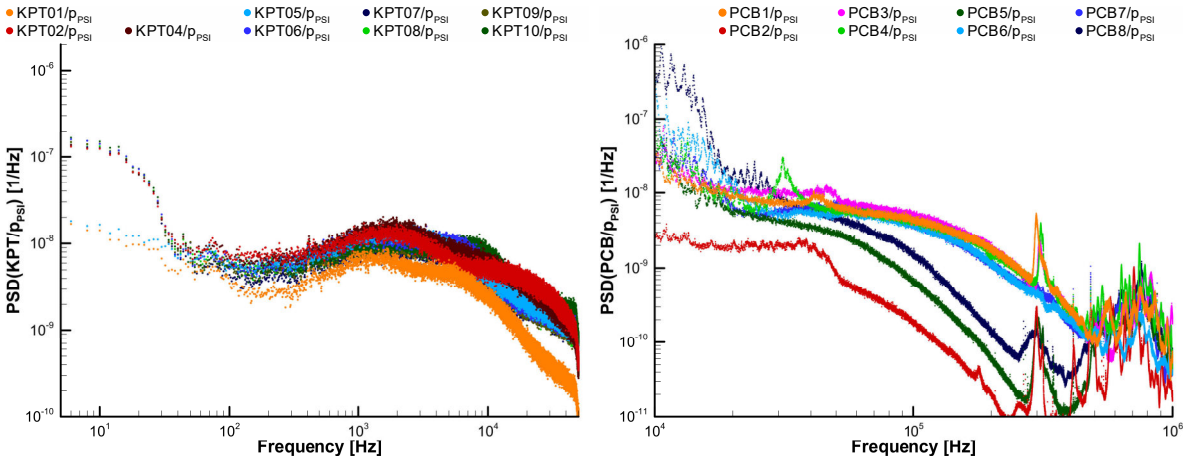

(b) run 19: $Ma_\infty = 5.298$, $Re_{\mathrm{u},\infty} = 6.070 \cdot 10^6 \, \frac{1}{\mathrm{m}}$, $\alpha = -0.20°$, $\beta = 0.25°$

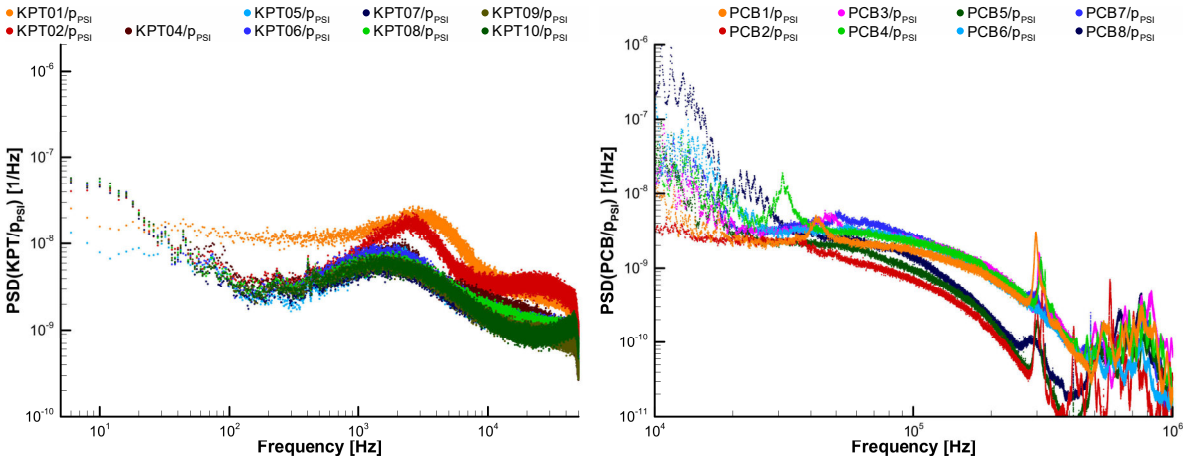

(c) run 20: $Ma_\infty = 5.317$, $Re_{\mathrm{u},\infty} = 11.944 \cdot 10^6 \, \frac{1}{\mathrm{m}}$, $\alpha = -0.20°$, $\beta = 0.25°$

Figure 3.7: Pressure spectra at $Ma_\infty = 5.3$ for various $Re_{\mathrm{u},\infty}$

increasing from PCB2 to PCB8.

Increasing the unit Reynolds number to $6 \cdot 10^6 \frac{1}{\mathrm{m}}$ leads to spectra shown in figure 3.7b. There are not two distinct groups for the KPT spectra any more, but most spectra now have an s-shape or inflection point close to 10 kHz. Again all sensors but KPT01 and KPT05 agree for frequencies lower than 30 Hz. On the right hand side the spectra of PCB1, PCB3, PCB4, PCB6 and PCB8 are almost identical at high amplitudes and hence probably all located in the turbulent region.

At $Re_{\mathrm{u},\infty} = 12 \cdot 10^6 \frac{1}{\mathrm{m}}$ (figure 3.7c) the spectra of KPT01 and KPT02 have a significant peak around 3 kHz and the other KPT a less prominent one at about 1.5 kHz. Again all sensors but KPT01 and KPT05 agree for frequencies lower than 30 Hz. The spectra of the PCB sensors look similar to those at $Re_{\mathrm{u},\infty} = 6 \cdot 10^6 \frac{1}{\mathrm{m}}$, but the amplitudes of the fringe sensors decreased and the central sensors moved closer together.

For $Ma_\infty = 6.0$ the spectra are similar and behave similar, but the observed phenomena occur further downstream or at higher at higher unit Reynolds number, since the boundary layer transition moves downstream. Figure 3.8a shows the results at $Re_{\mathrm{u},\infty} = 3 \cdot 10^6 \frac{1}{\mathrm{m}}$. The Kulite pressure transducers are again split in two groups and those in the symmetry plane reveal a double peak. For frequencies lower than 30 Hz just KPT03 shows different values, all other agree quite well. Just PCB04 shows a clear peak like a second (Mach) mode and PCB06 some remains. All other PCB measure the low amplitudes of a laminar boundary layer.

In figure 3.8b for $Re_{\mathrm{u},\infty} = 6 \cdot 10^6 \frac{1}{\mathrm{m}}$, there are still two groups for the KPT spectra, but KPT03, KPT04 and KPT05 moved to the upper one. The spectra of KPT01 and KPT02 still has a double peak in the high frequency range and those of KPT06 to KPT10 develop an inflection point close to 10 kHz. Here the values of all sensors agree in the low frequency range. PCB1, PCB4, PCB6 and PCB8 are almost identical at high amplitudes, but PCB3 observes significant lower amplitudes.

At $Re_{\mathrm{u},\infty} = 12 \cdot 10^6 \frac{1}{\mathrm{m}}$ (figure 3.8c) all Kulite pressure transducers show very similar results, just the spectra of KPT01 differ slightly and KPT02 as well as KPT03 show increased amplitudes for frequencies higher than 10 kHz. Now also the spectrum of PCB3 agrees with those of the other fringe sensors and the central sensors again moved closer together.

The transition is further delayed by increasing the Mach number to 7.0 as documented in figure 3.9. Again there are two groups for the high frequency range of the Kulite pressure transducers. At $Re_{\mathrm{u},\infty} = 3 \cdot 10^6 \frac{1}{\mathrm{m}}$ (figure 3.9a) KPT06 that was always in the upper group for the lower Mach numbers is now located just between both groups. At $Re_{\mathrm{u},\infty} = 6 \cdot 10^6 \frac{1}{\mathrm{m}}$ (figure 3.9b) KPT06 is again completely in the upper group and KPT05 as well as KPT04 seem to move upwards, too. In addition there is a small bump at 8 kHz for KPT07 to KPT10. At $Re_{\mathrm{u},\infty} = 12 \cdot 10^6 \frac{1}{\mathrm{m}}$ (figure 3.9c) just the spectrum of KPT01 does not agree with the others. For frequencies below 30 Hz all spectra agree at

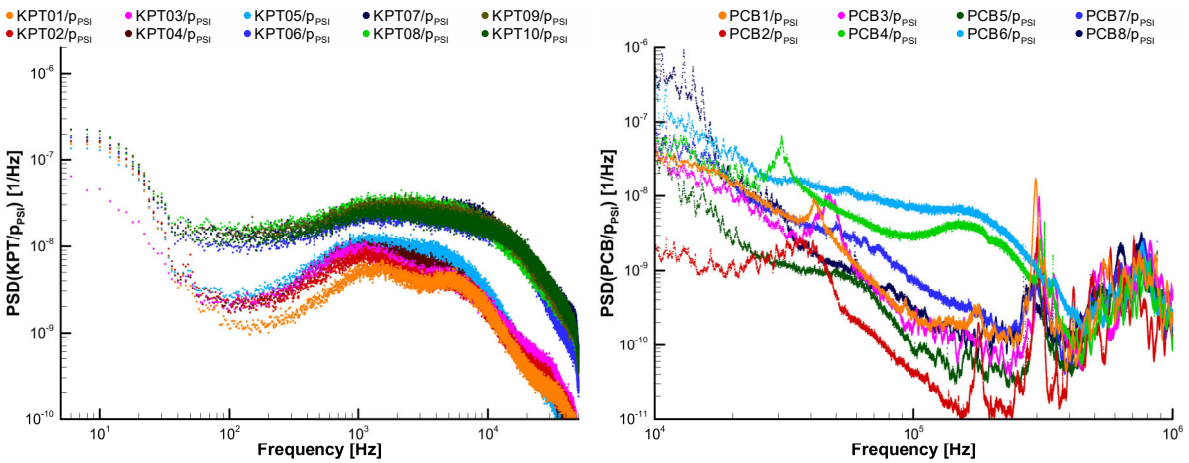

(a) run 3: $Ma_\infty = 5.986$, $Re_{\mathrm{u},\infty} = 3.025 \cdot 10^6 \, \frac{1}{\mathrm{m}}$, $\alpha = -0.20°$, $\beta = 0.25°$

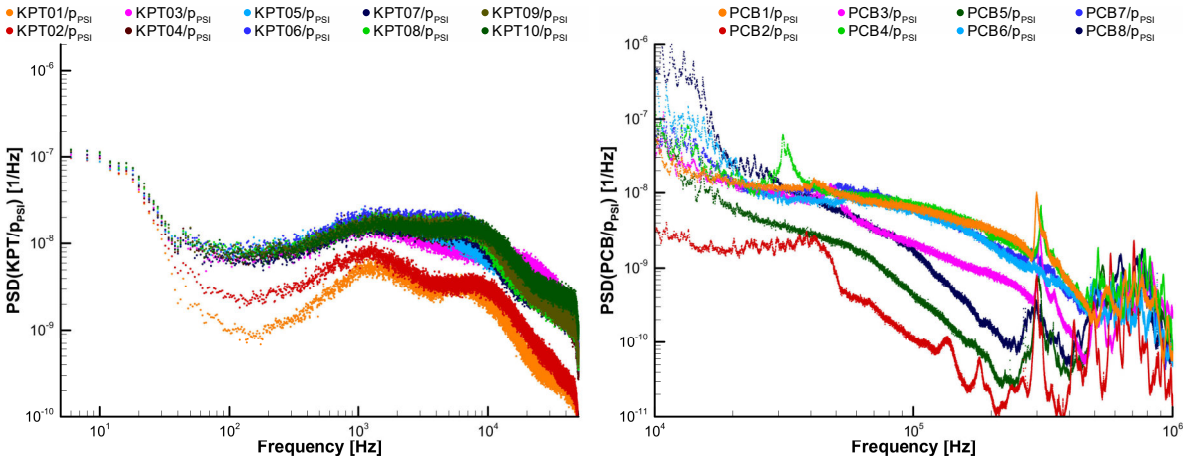

(b) run 4: $Ma_\infty = 6.017$, $Re_{\mathrm{u},\infty} = 5.963 \cdot 10^6 \, \frac{1}{\mathrm{m}}$, $\alpha = -0.20°$, $\beta = 0.25°$

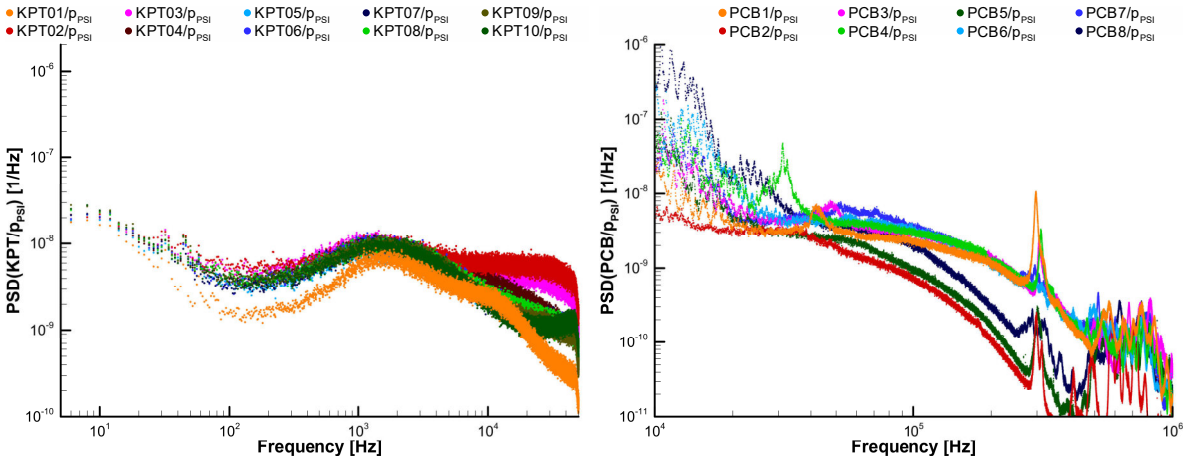

(c) run 5: $Ma_\infty = 6.054$, $Re_{\mathrm{u},\infty} = 11.725 \cdot 10^6 \, \frac{1}{\mathrm{m}}$, $\alpha = -0.20°$, $\beta = 0.25°$

Figure 3.8: Pressure spectra at $Ma_\infty = 6.0$ for various $Re_{\mathrm{u},\infty}$

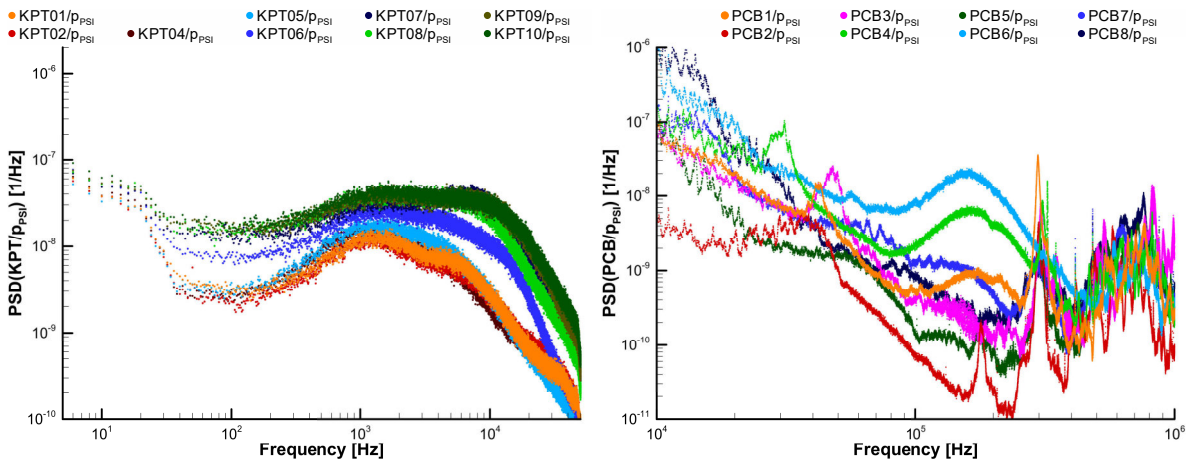

(a) run 23: $Ma_\infty = 7.013$, $Re_{\mathrm{u},\infty} = 3.076 \cdot 10^6 \, \frac{1}{\mathrm{m}}$, $\alpha = 0.00°$, $\beta = 0.00°$

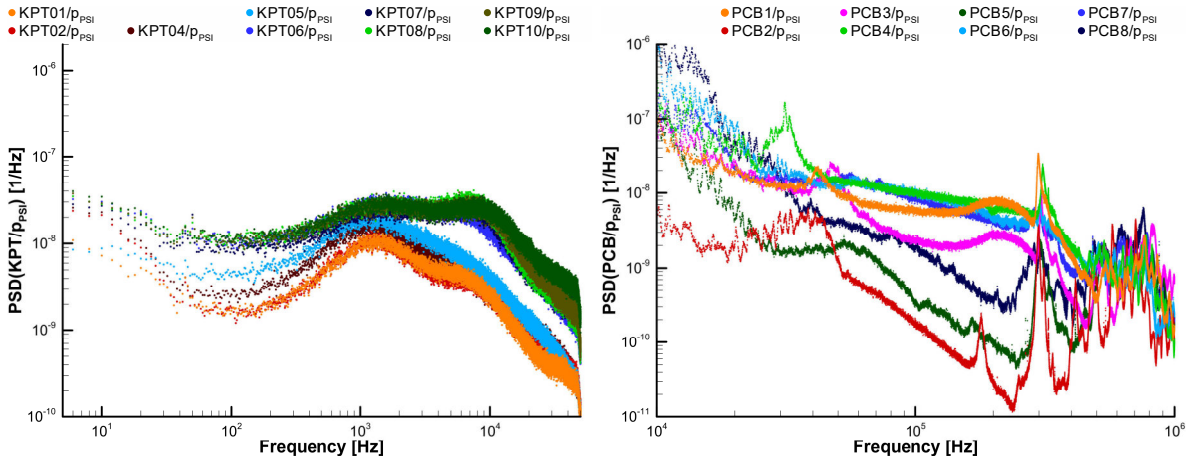

(b) run 24: $Ma_\infty = 7.047$, $Re_{\mathrm{u},\infty} = 5.915 \cdot 10^6 \, \frac{1}{\mathrm{m}}$, $\alpha = 0.00°$, $\beta = 0.00°$

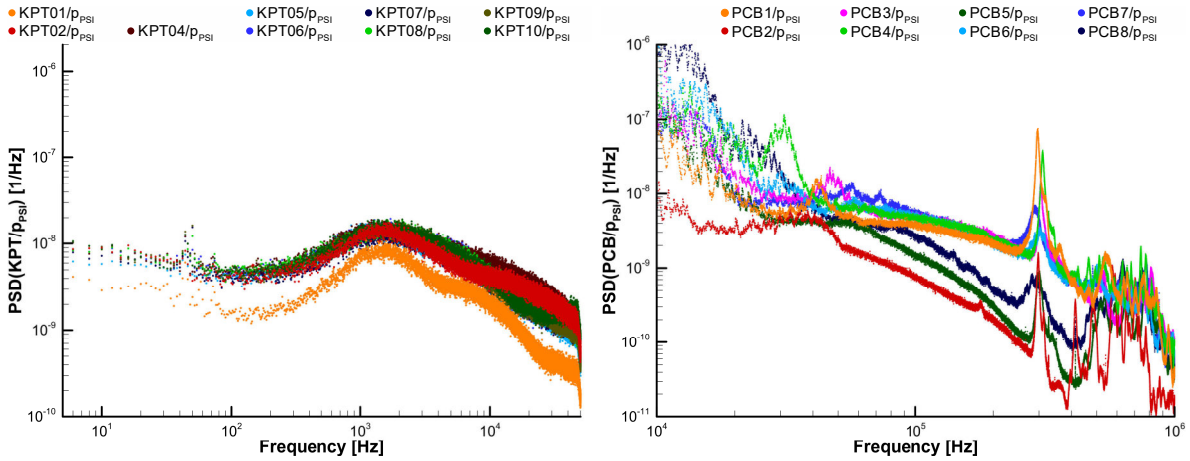

(c) run 25: $Ma_\infty = 7.104$, $Re_{\mathrm{u},\infty} = 12.106 \cdot 10^6 \, \frac{1}{\mathrm{m}}$, $\alpha = 0.00°$, $\beta = 0.00°$

Figure 3.9: Pressure spectra at $Ma_\infty = 7.0$ for various $Re_{\mathrm{u},\infty}$

$Re_{u,\infty} = 3 \cdot 10^6 \frac{1}{m}$, KPT01 and KPT05 differ at $Re_{u,\infty} = 6 \cdot 10^6 \frac{1}{m}$ and just KPT01 differs at $Re_{u,\infty} = 12 \cdot 10^6 \frac{1}{m}$.

The peaks similar to a second (Mach) mode are much more distinct in the PCB spectra at $Ma_\infty = 7.0$. At $Re_{u,\infty} = 3 \cdot 10^6 \frac{1}{m}$ it is present in the data of PCB1, PCB4 and PCB6 as can be seen in figure 3.9a. Along the way downstream the measured amplitude increases by more than factor 20 and the frequency slightly decreases from 170 kHz to 160 kHz. At $Re_{u,\infty} = 6 \cdot 10^6 \frac{1}{m}$ similar peaks are still present for PCB1 and PCB3. But PCB3 is probably at the beginning of the transition process and PCB1 at the end. PCB4, PCB6 and PCB7 reveal similar turbulent spectra. At $Re_{u,\infty} = 12 \cdot 10^6 \frac{1}{m}$ all fringe PCB reveal similar turbulent spectra.

3.2.4 Influence of angle of attack

The influence of the angle of attack α on the dynamic measurements of Kulite pressure transducers in the symmetry plane is documented in figure 3.10. On the left hand side for $Ma_\infty = 6.0$ and on the right hand side for $Ma_\infty = 7.0$. The first row includes measurements of KPT01 and the second row those of KPT02. The spectra agree quite well for frequencies above 30 Hz, but the secondary peak around 5 kHz at $Ma_\infty = 6.0$ is just present for $|\alpha| \leq 4°$. At $Ma_\infty = 7.0$ there are differences for frequencies higher than 10 kHz. The spectra differ more in the low frequency range, especially for KPT01 at $Ma_\infty = 7.0$ also with a clear trend – higher amplitudes for higher α. In contrast to that they almost agree for KPT02 at $Ma_\infty = 7.0$.

For the KPT off the symmetry plane the effect of the angle of attack depends on the z position of the sensor, as shown in figure 3.11. For KPT05 the results are similar to those in the symmetry plane – just an effect for frequencies below 30 Hz and a small effect for frequencies above 10 kHz. But for KPT06 at $Ma_\infty = 6.0$ and KPT07 at $Ma_\infty = 7.0$ an additional peak forms around 7.5 kHz. While it is pronounced at 3.8° and weak at 1.8° and 6.0° for $Ma_\infty = 6.0$ it is pronounced at 2.0° and 4.0° and weak at 0.0° and 8.0° for $Ma_\infty = 7.0$.

The development of the second (Mach) mode like peak can be followed in the spectra of the fringe PCB for various angle of attack. In figure 3.12 measurements at $Ma_\infty = 6.0$ are on the left hand side and those at $Ma_\infty = 7.0$ on the right hand side. The first row contains data from the first fringe sensor PCB1 at $x = 287.500$ mm, the second row of PCB4 at $x = 343.750$ mm and the last row of the last fringe sensor PCB6 at $x = 397.500$ mm. At ±8° and for $Ma_\infty = 6.0$ also at −4.2° no second (Mach) mode like peak could be measured. Nevertheless in the data of PCB1 at $Ma_\infty = 6.0$ for −0.2° to 3.8° and at $Ma_\infty = 7.0$ for −4° to 4° such a peak can be identified for frequencies from 100 kHz to 200 kHz. They are all amplified until PCB4 while the frequency slightly decrease. At $Ma_\infty = 6.0$ also for −2.2° and 6.0° a second (Mach) mode like peak is

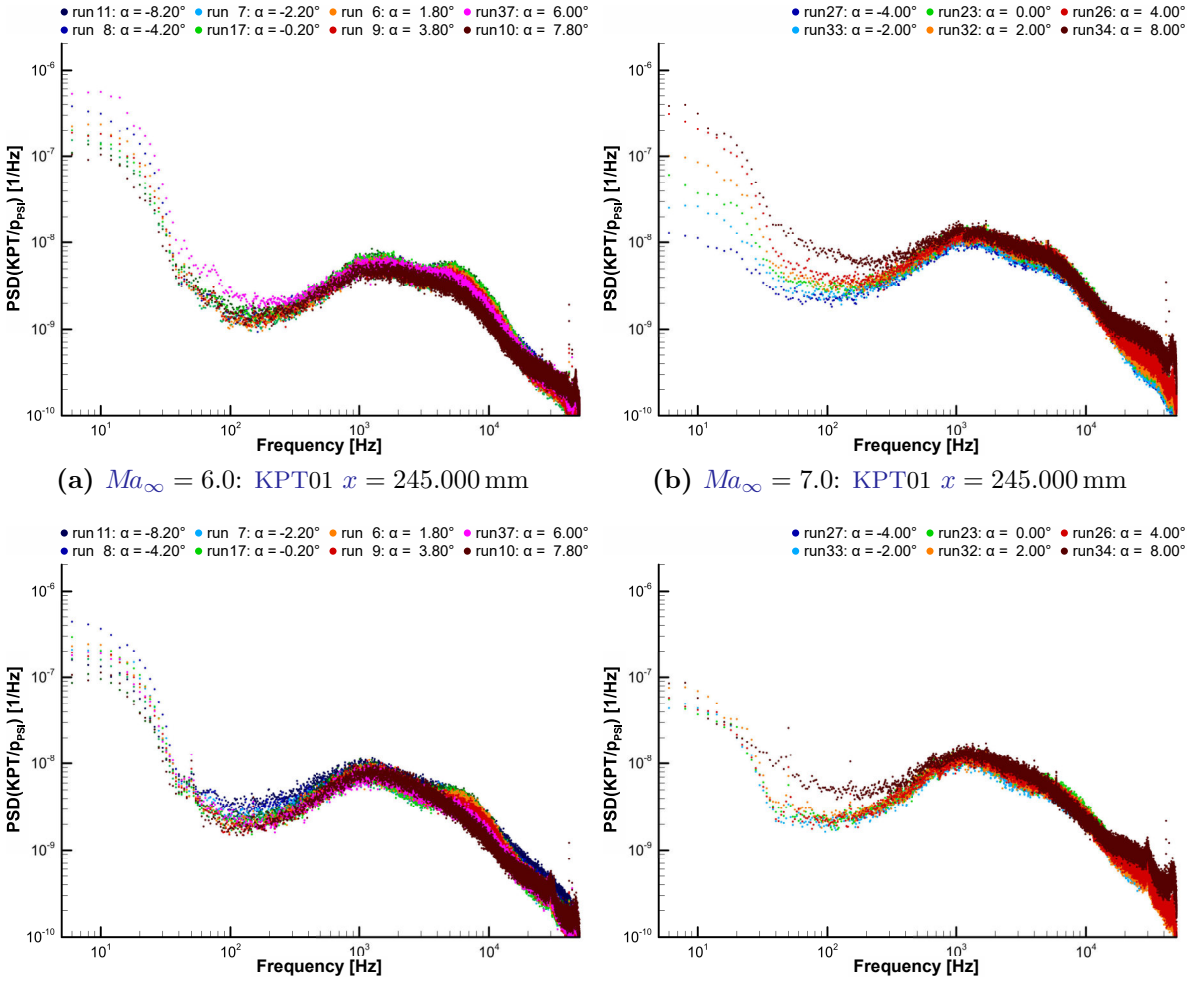

(a) $Ma_\infty = 6.0$: KPT01 $x = 245.000\,\mathrm{mm}$ **(b)** $Ma_\infty = 7.0$: KPT01 $x = 245.000\,\mathrm{mm}$

(c) $Ma_\infty = 6.0$: KPT02 $x = 320.000\,\mathrm{mm}$ **(d)** $Ma_\infty = 7.0$: KPT02 $x = 320.000\,\mathrm{mm}$

Figure 3.10: Spectra of KPT in the symmetry plane for various α

detected. The spectra of PCB6 at $-4°$ and $-2°$ are those of turbulent boundary layer for $Ma_\infty = 6.0$ and also almost at $Ma_\infty = 7.0$. But for $0°$ to $6°$ there are still pronounced peaks for both Mach numbers.

3.2.5 Influence of yaw angle

There is not much influence of the yaw angle β on the spectra of the Kulite pressure transducers in the symmetry plane, as shown in figure 3.13. Just the values below 30 Hz vary and the notch around 3 kHz vanishes for non zero angles. In contrast to that there is a significant effect of β onto the KPT off the symmetry plane (figure 3.14). For KPT05

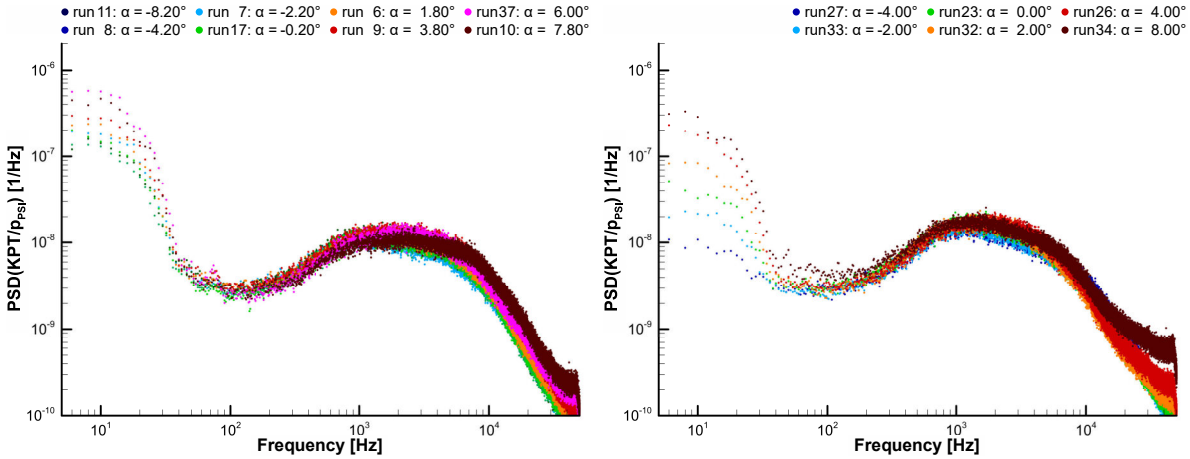

(a) $Ma_\infty = 6.0$: KPT05 $z = 20.000\,\mathrm{mm}$

(b) $Ma_\infty = 7.0$: KPT05 $z = 20.000\,\mathrm{mm}$

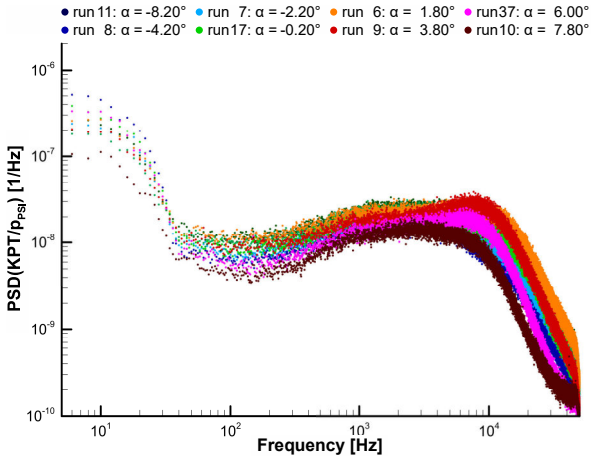

(c) $Ma_\infty = 6.0$: KPT06 $z = 40.500\,\mathrm{mm}$

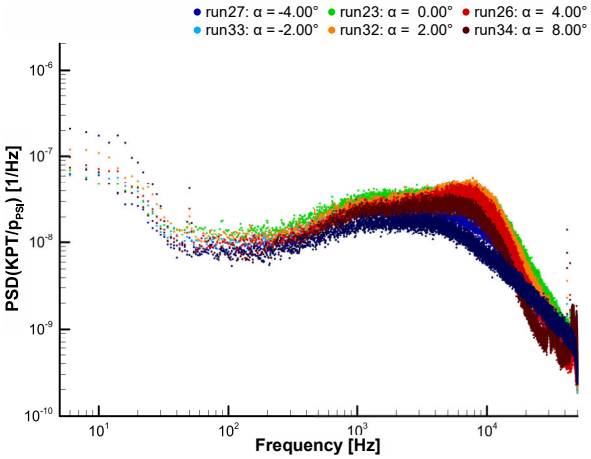

(d) $Ma_\infty = 7.0$: KPT07 $z = 53.500\,\mathrm{mm}$

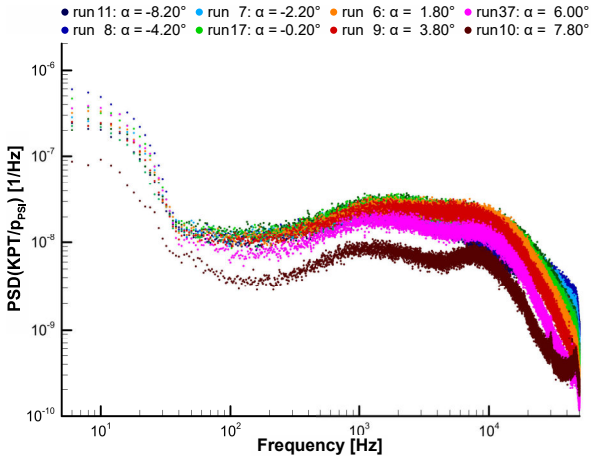

(e) $Ma_\infty = 6.0$: KPT10 $z = 80.000\,\mathrm{mm}$

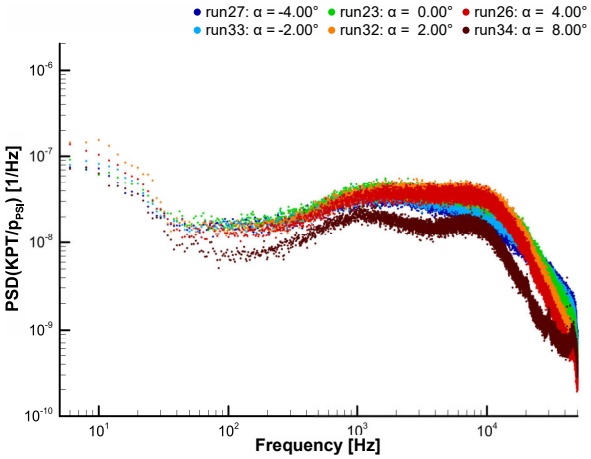

(f) $Ma_\infty = 7.0$: KPT10 $z = 80.000\,\mathrm{mm}$

Figure 3.11: Spectra of KPT off the symmetry plane at $x = 395\,\mathrm{mm}$ for various α

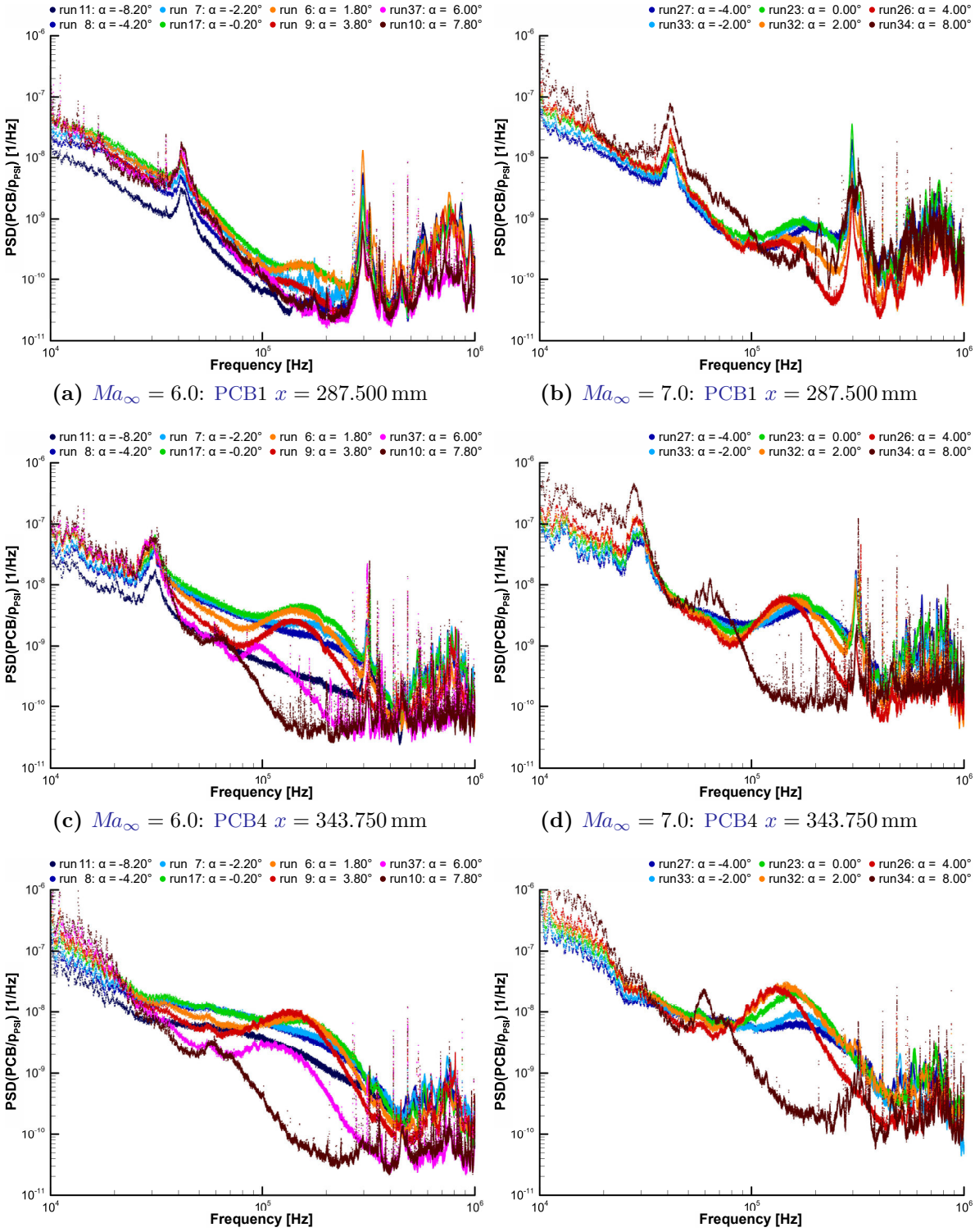

(a) $Ma_\infty = 6.0$: PCB1 $x = 287.500\,\mathrm{mm}$ **(b)** $Ma_\infty = 7.0$: PCB1 $x = 287.500\,\mathrm{mm}$

(c) $Ma_\infty = 6.0$: PCB4 $x = 343.750\,\mathrm{mm}$ **(d)** $Ma_\infty = 7.0$: PCB4 $x = 343.750\,\mathrm{mm}$

(e) $Ma_\infty = 6.0$: PCB6 $x = 397.500\,\mathrm{mm}$ **(f)** $Ma_\infty = 7.0$: PCB6 $x = 397.500\,\mathrm{mm}$

Figure 3.12: Pressure spectra of fringe PCB for various α

from $-2°$ to $4°$ the amplitudes in the spectra increase for frequencies above 30 Hz, but there the spectra at $-4°$ and $-2°$ are more or less identical. For the lower frequencies the amplitudes decrease with increasing β at $Ma_\infty = 7.0$ and split into two the groups $\pm 4°$ and $-2°$ to $2°$ at $Ma_\infty = 6.0$. For KPT07 the increase in the high frequency range is observable for β from $-4°$ to $0°$ and the amplitudes agree quite well in the low frequency range. The spectra from $0°$ to $4°$ agree quite well, but there is a peak around 8 kHz for $\beta = 0°$, which does not exist in the other spectra. The spectra of KPT10 are more or less the same for all values of β.

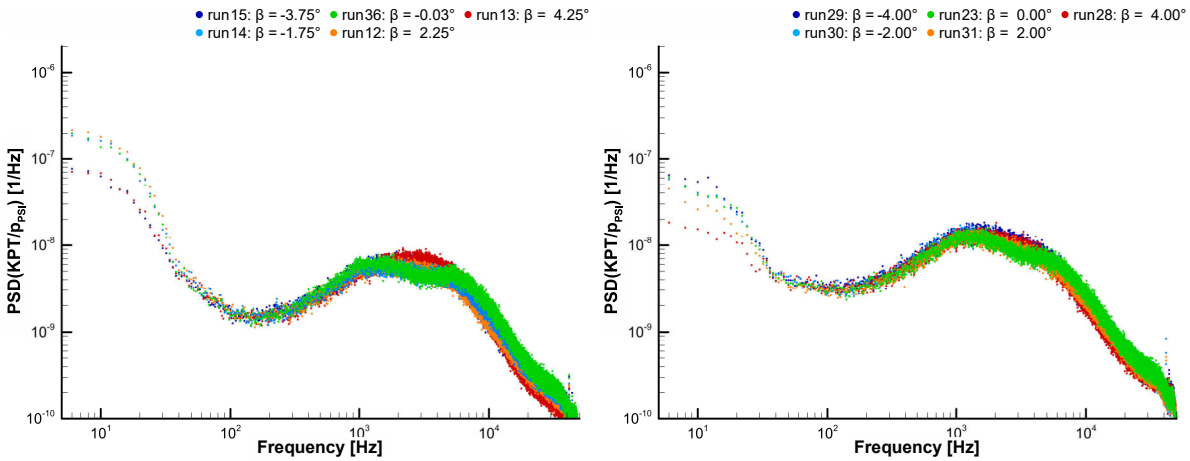

(a) $Ma_\infty = 6.0$: KPT01 $x = 245.000$ mm

(b) $Ma_\infty = 7.0$: KPT01 $x = 245.000$ mm

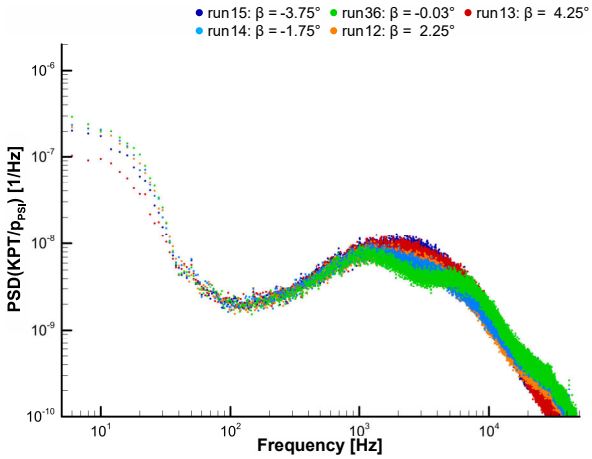

(c) $Ma_\infty = 6.0$: KPT02 $x = 320.000$ mm

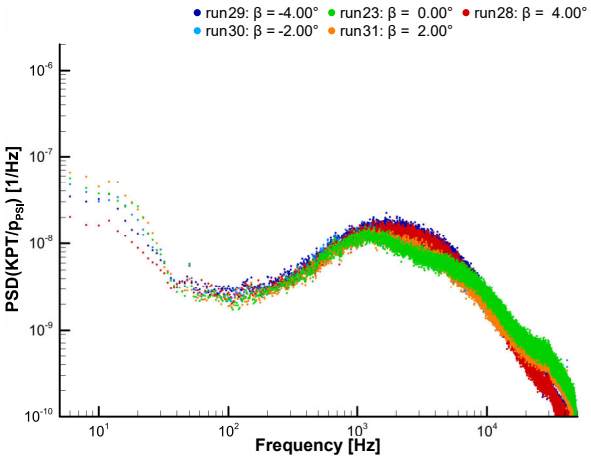

(d) $Ma_\infty = 7.0$: KPT02 $x = 320.000$ mm

Figure 3.13: Spectra of KPT in the symmetry plane for various β

The second (Mach) mode like peak is present in all spectra of the fringe PCB for β from $-4°$ to $0°$, shown in figure 3.15. For PCB1 the amplitudes of the spectrum at $\beta = -4°$ are higher than those for $-2°$ and $0°$, which are quite similar. For PCB4 the amplitudes

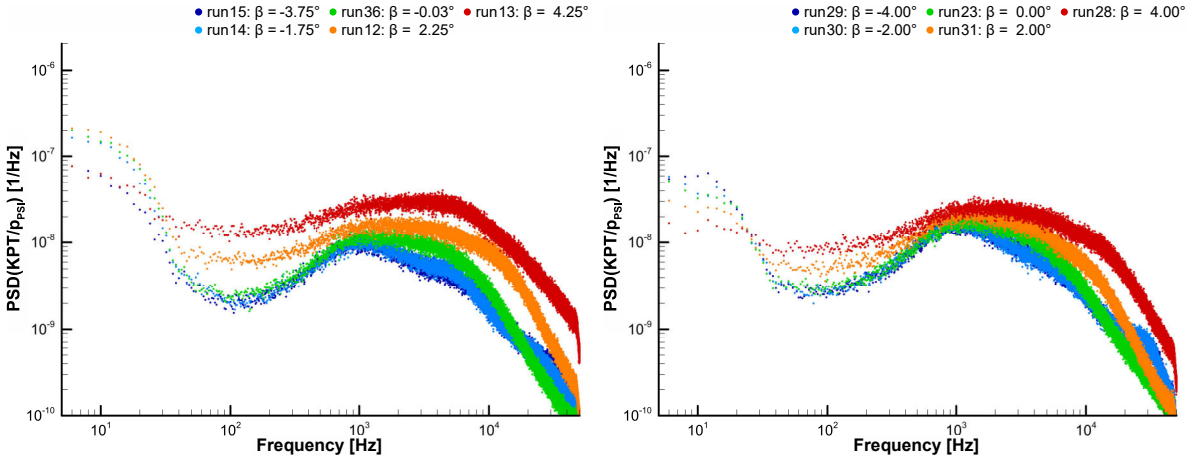

(a) $Ma_\infty = 6.0$: KPT05 $z = 20.000\,\mathrm{mm}$

(b) $Ma_\infty = 7.0$: KPT05 $z = 20.000\,\mathrm{mm}$

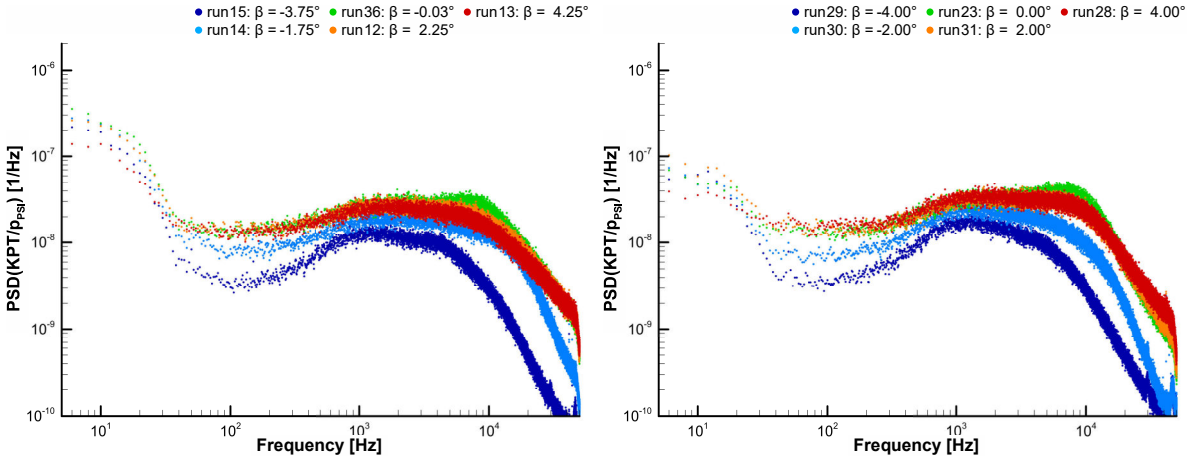

(c) $Ma_\infty = 6.0$: KPT07 $z = 53.500\,\mathrm{mm}$

(d) $Ma_\infty = 7.0$: KPT07 $z = 53.500\,\mathrm{mm}$

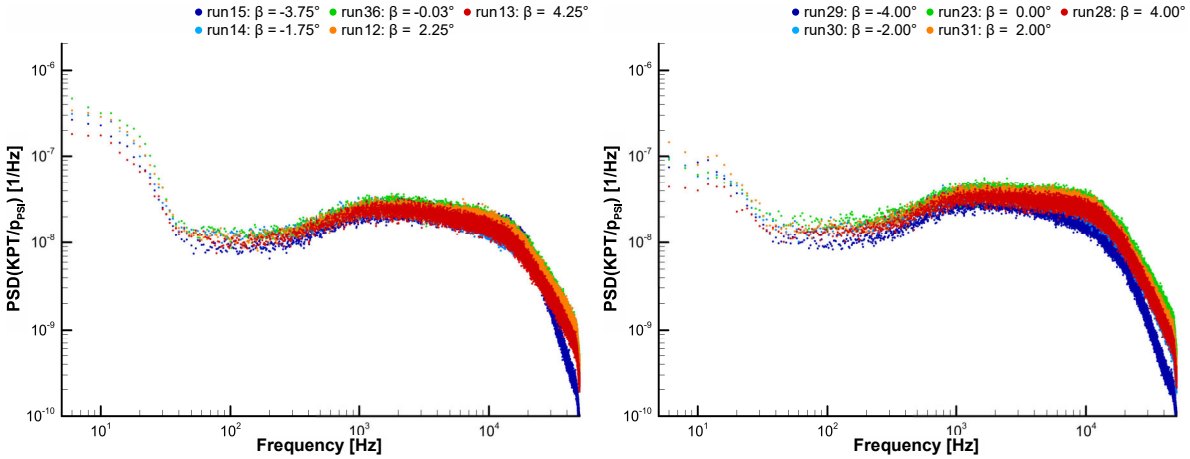

(e) $Ma_\infty = 6.0$: KPT10 $z = 80.000\,\mathrm{mm}$

(f) $Ma_\infty = 7.0$: KPT10 $z = 80.000\,\mathrm{mm}$

Figure 3.14: Spectra of KPT off the symmetry plane at $x = 395\,\mathrm{mm}$ for various β

of the spectrum at $\beta = -2°$ are slightly higher and those at 0° and slightly lower than those at −4°. For the PCB6 the spectra for β from −4° to 0° agree quite well. While it almost vanished for $Ma_\infty = 6.0$ it is still pronounced at $Ma_\infty = 7.0$. PCB6 also detects a similar peak for $\beta = 2°$, which besides that just observable at PCB4 for $Ma_\infty = 7.0$.

Figure 3.16 reveals that the intermediate PCB – which are PCB3 and PCB7 – detect just very weak peaks similar to a second (Mach) mode at $Ma_\infty = 7.0$ for $\beta = 0°$. But for β equal to −4° and −2° there is a distinct peak although it almost vanished on PCB7 for $Ma_\infty = 6.0$. For β equal to 2° and 4° there are no similar peak for these sensors.

3.3 Surface heating

The analysis of the surface temperature measurements, in this report is still a preliminary one, as the mapping on 3D surfaces and the computation of heat fluxes or Stanton numbers could not be performed, yet. Nevertheless the observations are interesting and may provide some further insights into the transition process. The plots within this section show the increase of the temperature on the top side of the model within 10 s from the wind tunnel start. The colour scale is manually adjusted to keep similar features in similar colours.

3.3.1 Reynolds number and Mach number effect

Figures 3.17 to 3.19 show for Ma_∞ equal to 5.3, 6.0 and 7.0 and $Re_{u,\infty}$ equal to $3 \cdot 10^6 \frac{1}{m}$, $6 \cdot 10^6 \frac{1}{m}$ and $12 \cdot 10^6 \frac{1}{m}$ the temperature increase on the model top side. Three zones can be identified.

The first zone is the central zone around the symmetry plane with no or very low temperature increase. It contracts along the model downstream. The contraction is increased by increasing the Reynolds number or decreasing the Mach number. For $Ma_\infty = 5.3$ it shrinks to approximately half width until the model end at $Re_{u,\infty} = 3 \cdot 10^6 \frac{1}{m}$ in figure 3.17a, it ends before KPT03 ($x = 395\,\text{mm}$) at $Re_{u,\infty} = 6 \cdot 10^6 \frac{1}{m}$ in figure 3.17b and ends before KPT02 ($x = 320\,\text{mm}$) at $Re_{u,\infty} = 12 \cdot 10^6 \frac{1}{m}$ in figure 3.17b. For $Ma_\infty = 6.0$ it shrinks to approximately two thirds width until the model end at $Re_{u,\infty} = 3 \cdot 10^6 \frac{1}{m}$ in figure 3.18a, it almost ends at the end of the model at $Re_{u,\infty} = 6 \cdot 10^6 \frac{1}{m}$ in figure 3.18b and ends before KPT03 ($x = 395\,\text{mm}$) at $Re_{u,\infty} = 12 \cdot 10^6 \frac{1}{m}$ in figure 3.18c. For $Ma_\infty = 7.0$ it just slightly shrinks at $Re_{u,\infty} = 3 \cdot 10^6 \frac{1}{m}$ in figure 3.19a, it shrinks to approximately half width until the model end at $Re_{u,\infty} = 6 \cdot 10^6 \frac{1}{m}$ in figure 3.19b and ends just before the model end at $Re_{u,\infty} = 12 \cdot 10^6 \frac{1}{m}$ in figure 3.19c.

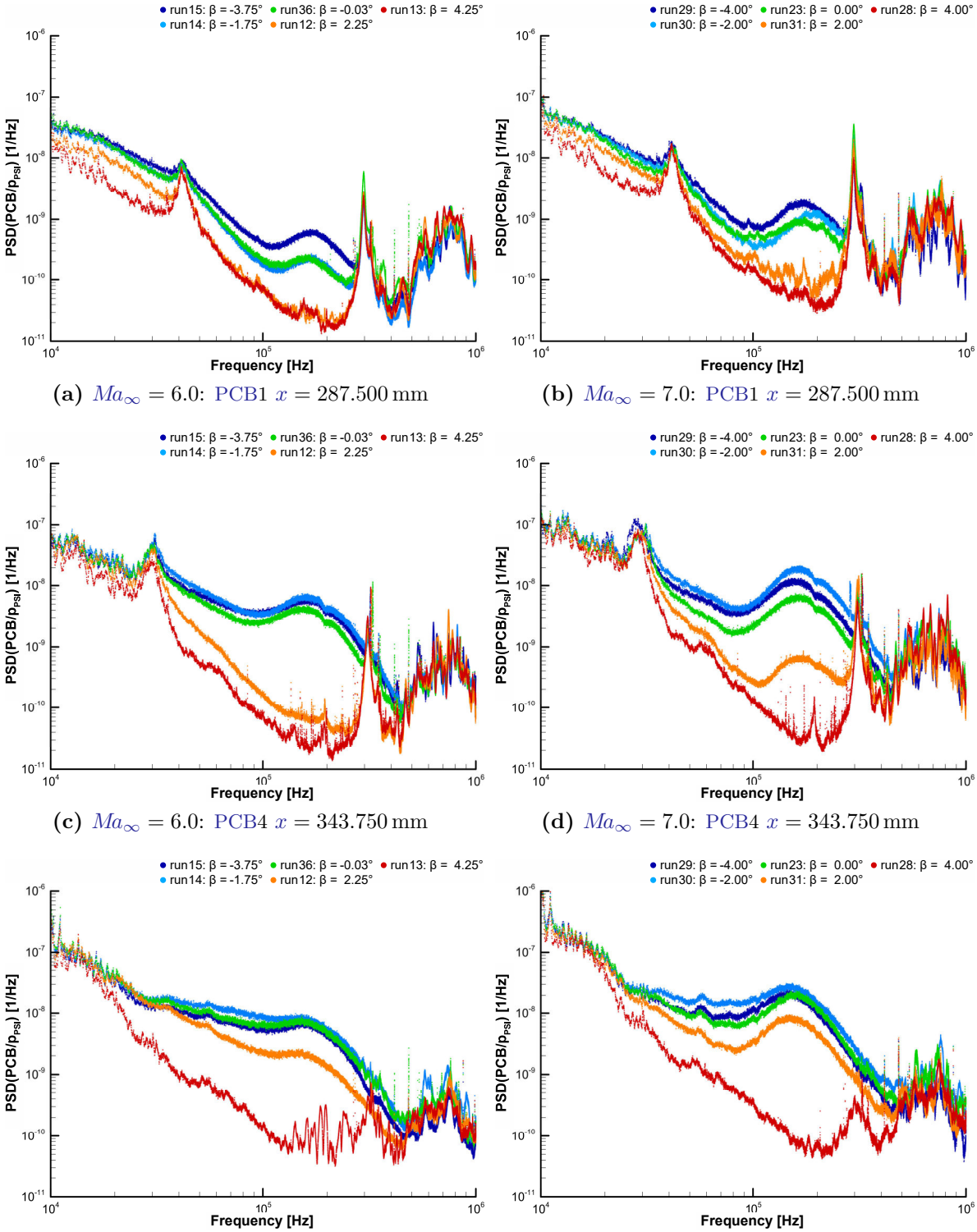

(a) $Ma_\infty = 6.0$: PCB1 $x = 287.500\,\mathrm{mm}$ **(b)** $Ma_\infty = 7.0$: PCB1 $x = 287.500\,\mathrm{mm}$

(c) $Ma_\infty = 6.0$: PCB4 $x = 343.750\,\mathrm{mm}$ **(d)** $Ma_\infty = 7.0$: PCB4 $x = 343.750\,\mathrm{mm}$

(e) $Ma_\infty = 6.0$: PCB6 $x = 397.500\,\mathrm{mm}$ **(f)** $Ma_\infty = 7.0$: PCB6 $x = 397.500\,\mathrm{mm}$

Figure 3.15: Pressure spectra of fringe PCB for various β

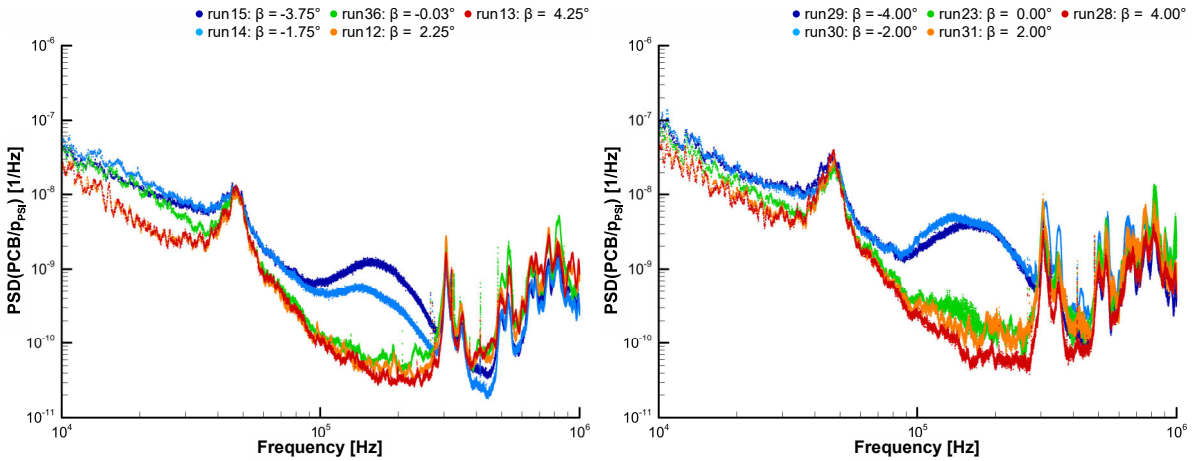

(a) $Ma_\infty = 6.0$: PCB3 $x = 307.500\,\mathrm{mm}$

(b) $Ma_\infty = 7.0$: PCB3 $x = 307.500\,\mathrm{mm}$

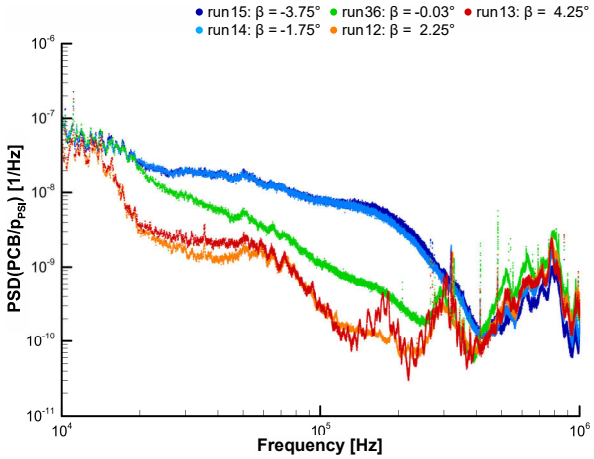

(c) $Ma_\infty = 6.0$: PCB7 $x = 397.500\,\mathrm{mm}$

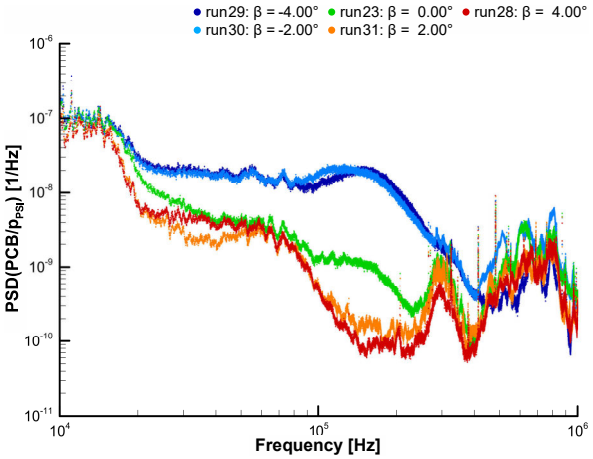

(d) $Ma_\infty = 7.0$: PCB7 $x = 397.500\,\mathrm{mm}$

Figure 3.16: Pressure spectra of intermediate PCB for various β

The second zone are the two wedge-shaped transition regions. Their tips are roughly in the middle between the model edge and the symmetry plane and they move upstream with increasing Reynolds number. They widen downstream until they fill the complete width of the surface. Figures 3.17 to 3.19 show that these regions move slightly downstream with increasing Mach number, but the optical localisation also depends on the choice of the colour scale. Therefore exact transition locations would need a comparison between the measured Stanton numbers and theoretic/simulated values for laminar and turbulent boundary layers.

The third zone lays between the central zone and the transition region and is characterized by streaky structures. It is not observable for $Ma_\infty = 7.0$ at $Re_{\mathrm{u},\infty} = 3 \cdot 10^6\ \frac{1}{\mathrm{m}}$ in figure 3.19a and almost displaced by the transition regions for $Ma_\infty = 5.3$ at $Re_{\mathrm{u},\infty} = 12 \cdot 10^6\ \frac{1}{\mathrm{m}}$

in figure 3.17c. But for the other cases it is quite distinct.

3.3.2 Influence of angle of attack

The influence of the angle of attack on the temperature increase of the top side is documented in figures 3.20 and 3.21. The left hand side includes the measurements at $Ma_\infty = 6.0$ and the right hand side those at $Ma_\infty = 7.0$.

For negative α the model top side is the windward side. For large negative α such as $-8°$ and $-4°$, secondary cold zones form parallel to the central zone as can be seen in figures 3.20a to 3.20c. It seems, that the more distinct those regions are the less distinct are the smaller streaky structures and the less is the evidence for second (Mach) modes in the PCB spectra.

For positive α the model top side is the leeward side. For large positive α such as $8°$ and $6°$ additional streaks on the top surface arise, that look like the footprint of large vortices originated at the "corners" of the leading edge (see figures 3.21e to 3.21g). The more those structures emerge the less the wedge-shaped transition regions can be identified. Also for these cases there are no or just very weak second (Mach) mode like peaks in the PCB spectra.

3.3.3 Influence of yaw angle

Figure 3.22 shows, that a change of the yaw angle leads primarily to a lateral shift of the zones on the top side and secondary also to a change of the observable flow features. While the Kulite pressure transducers in the symmetry plane are usually located inside the central zone, KPT02 and KPT03 leave that zone for $\beta = \pm 4°$. Also PCB2, PCB5 and PCB8, which are usually inside the central zone leave it for β equal to $-4°$ and $-2°$. In contrast to that PCB3 and PCB7 are usually far outside the central zone, but for $\beta = 4°$ they are inside or right at the border.

Also the streaky zone shifts with β, but the streaks also seem to become less pronounced for larger values of β. The transition zone becomes broader on the windward side and narrower on the leeward side. When it becomes broader on the PCB side for β equal to $-4°$ and $-2°$ as in figures 3.22a to 3.22d PCB3 and PCB7 also detect second (Mach) mode like peaks as shown in figure 3.16. For $\beta = -4°$ the transition zone seems to vanish completely on the KPT side and for $\beta = 4°$ it seems to vanish on the PCB side.

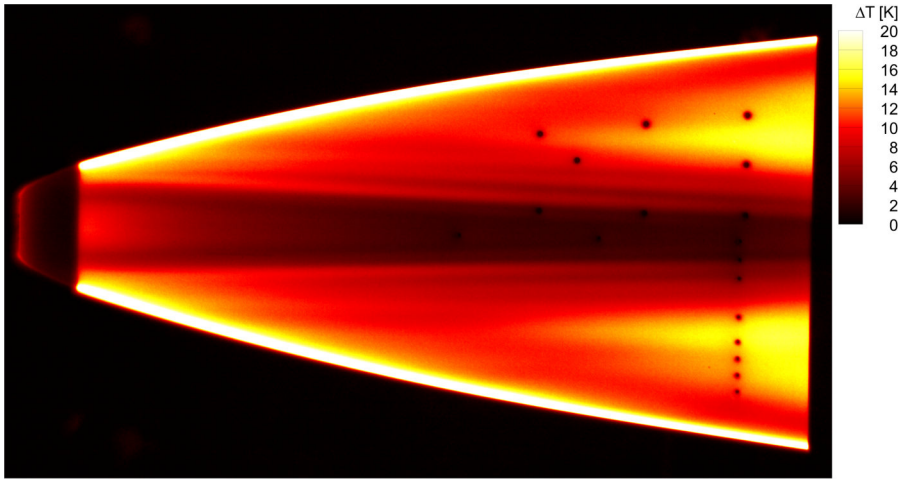

(a) run 18: $Ma_\infty = 5.276$, $Re_{\mathrm{u},\infty} = 3.059 \cdot 10^6 \, \frac{1}{\mathrm{m}}$, $\alpha = -0.20°$, $\beta = 0.25°$

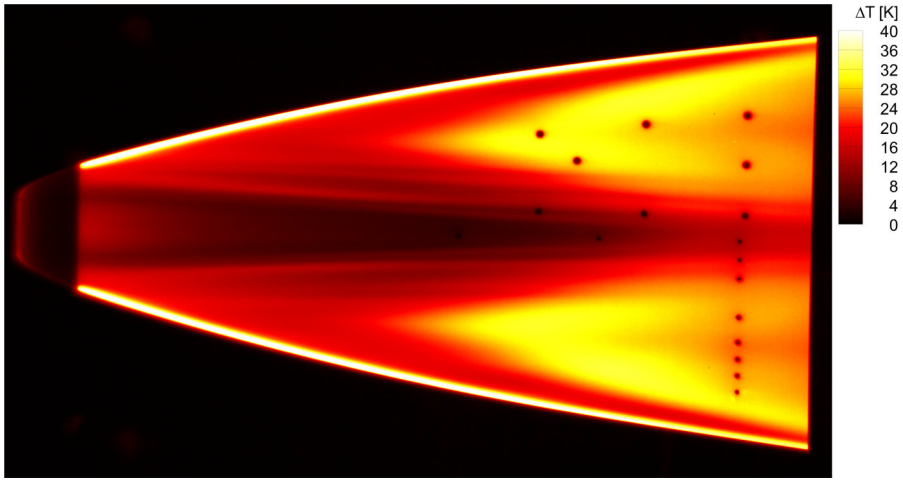

(b) run 19: $Ma_\infty = 5.298$, $Re_{\mathrm{u},\infty} = 6.070 \cdot 10^6 \, \frac{1}{\mathrm{m}}$, $\alpha = -0.20°$, $\beta = 0.25°$

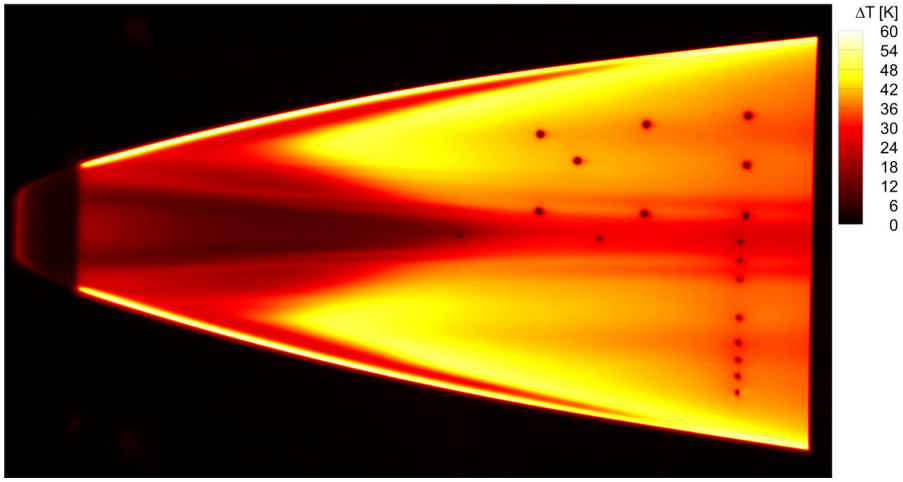

(c) run 20: $Ma_\infty = 5.317$, $Re_{\mathrm{u},\infty} = 11.944 \cdot 10^6 \, \frac{1}{\mathrm{m}}$, $\alpha = -0.20°$, $\beta = 0.25°$

Figure 3.17: Surface temperature increase at $Ma_\infty = 5.3$ for various $Re_{\mathrm{u},\infty}$

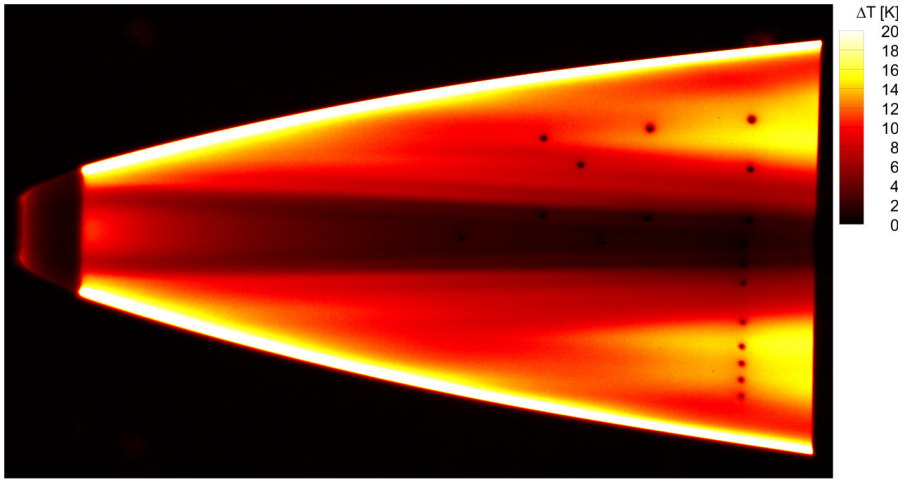

(a) run 3: $Ma_\infty = 5.986$, $Re_{\mathrm{u},\infty} = 3.025 \cdot 10^6 \, \frac{1}{\mathrm{m}}$, $\alpha = -0.20°$, $\beta = 0.25°$

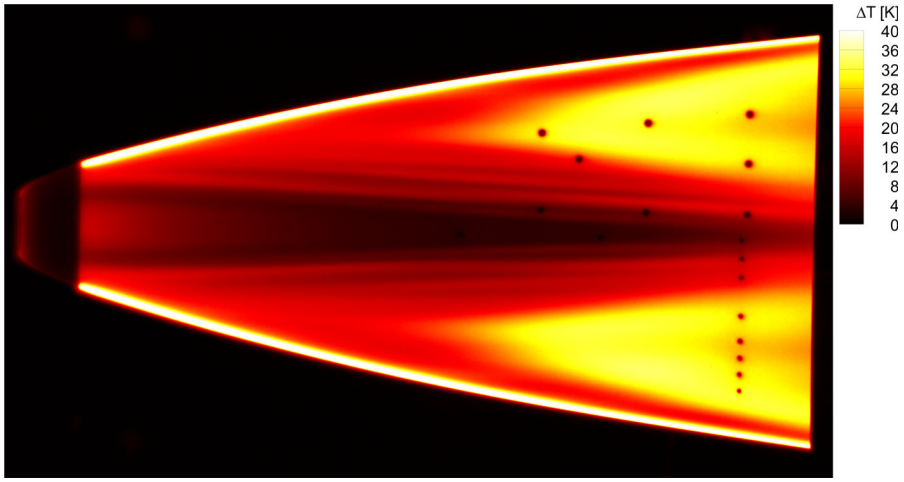

(b) run 4: $Ma_\infty = 6.017$, $Re_{\mathrm{u},\infty} = 5.963 \cdot 10^6 \, \frac{1}{\mathrm{m}}$, $\alpha = -0.20°$, $\beta = 0.25°$

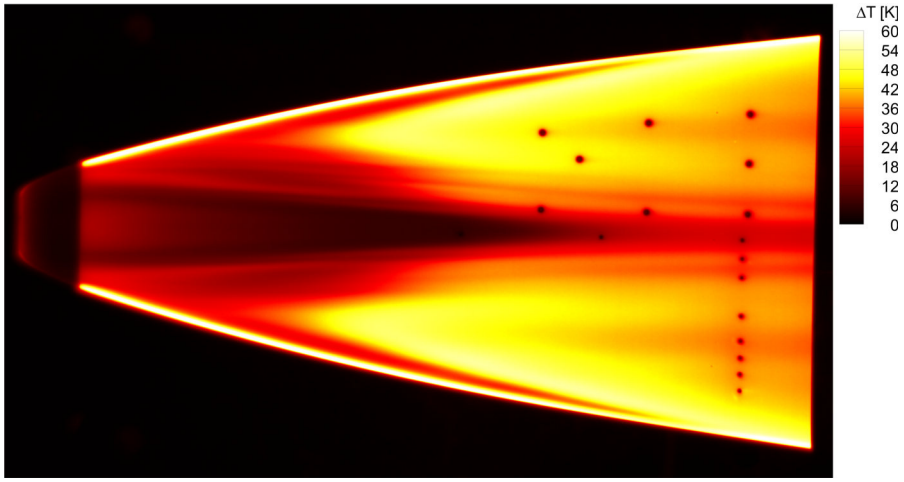

(c) run 5: $Ma_\infty = 6.054$, $Re_{\mathrm{u},\infty} = 11.725 \cdot 10^6 \, \frac{1}{\mathrm{m}}$, $\alpha = -0.20°$, $\beta = 0.25°$

Figure 3.18: Surface temperature increase at $Ma_\infty = 6.0$ for various $Re_{\mathrm{u},\infty}$

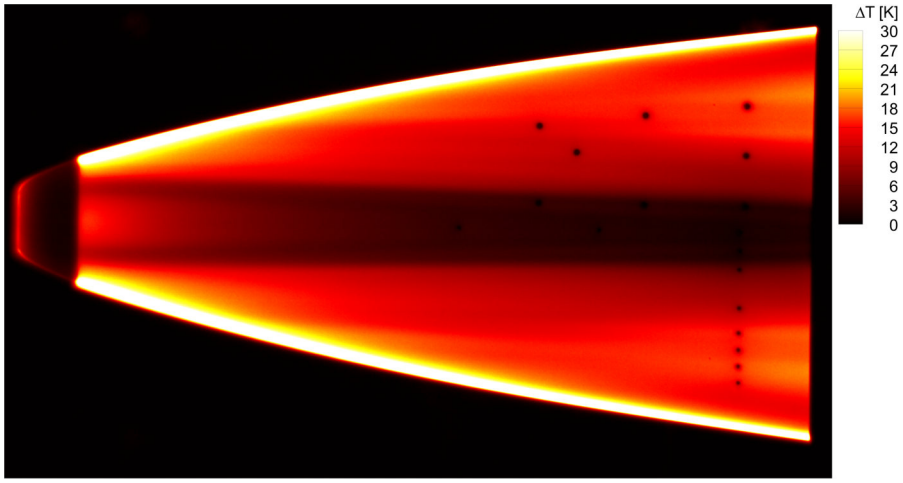

(a) run 23: $Ma_\infty = 7.013$, $Re_{\mathrm{u},\infty} = 3.076 \cdot 10^6 \, \frac{1}{\mathrm{m}}$, $\alpha = 0.00°$, $\beta = 0.00°$

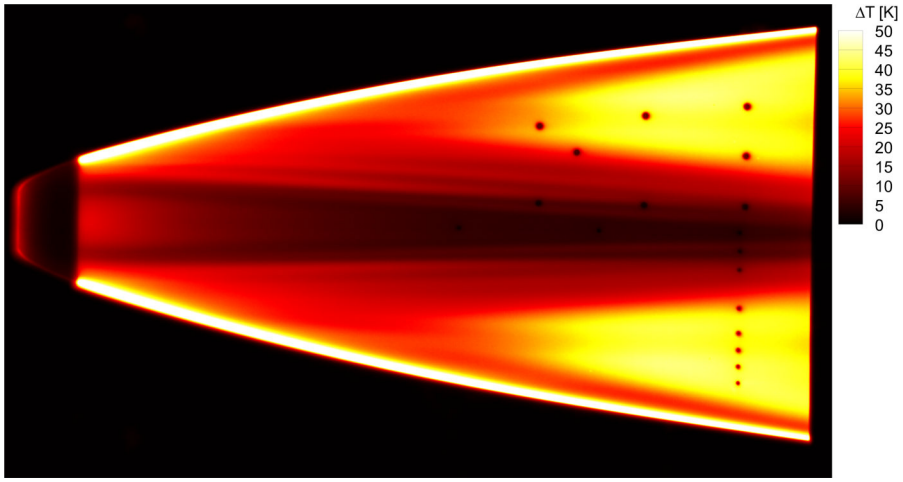

(b) run 24: $Ma_\infty = 7.047$, $Re_{\mathrm{u},\infty} = 5.915 \cdot 10^6 \, \frac{1}{\mathrm{m}}$, $\alpha = 0.00°$, $\beta = 0.00°$

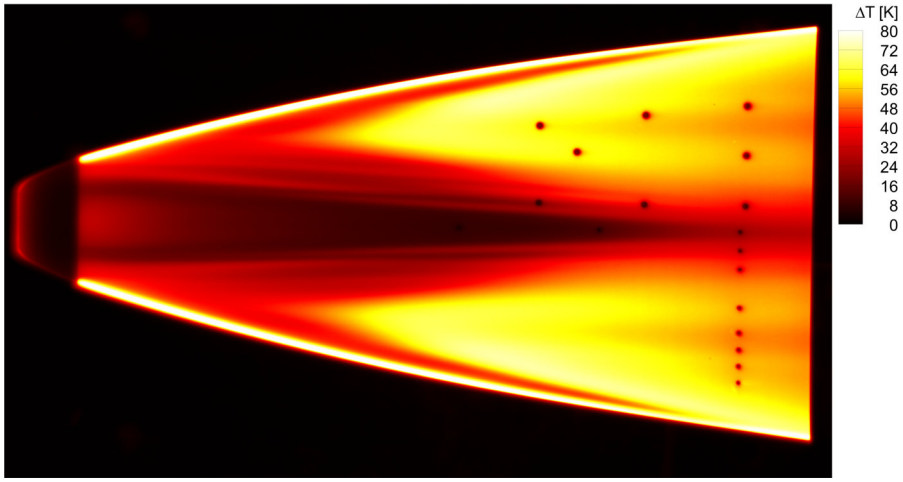

(c) run 25: $Ma_\infty = 7.104$, $Re_{\mathrm{u},\infty} = 12.106 \cdot 10^6 \, \frac{1}{\mathrm{m}}$, $\alpha = 0.00°$, $\beta = 0.00°$

Figure 3.19: Surface temperature increase at $Ma_\infty = 7.0$ for various $Re_{\mathrm{u},\infty}$

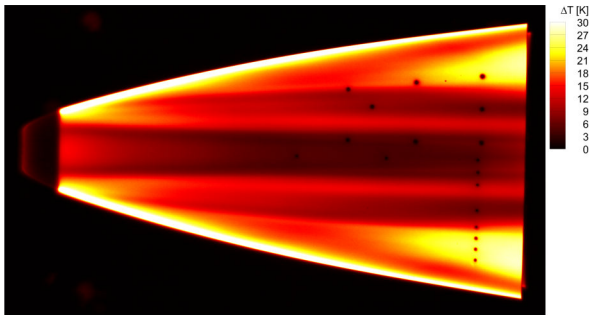

(a) run 11: $Ma_\infty = 5.987$, $\alpha = -8.20°$

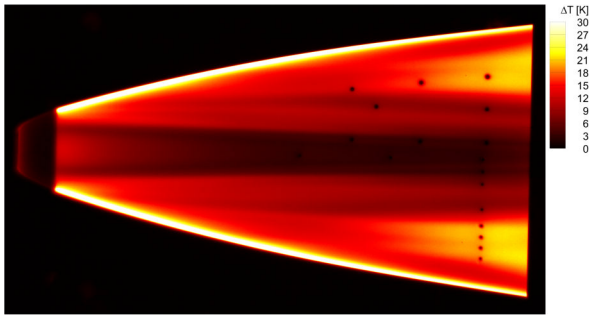

(b) run 8: $Ma_\infty = 5.987$, $\alpha = -4.20°$

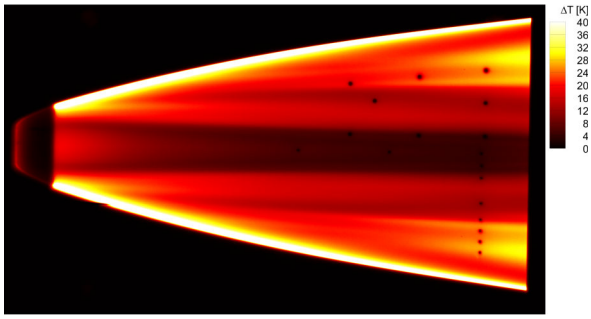

(c) run 27: $Ma_\infty = 7.013$, $\alpha = -4.00°$

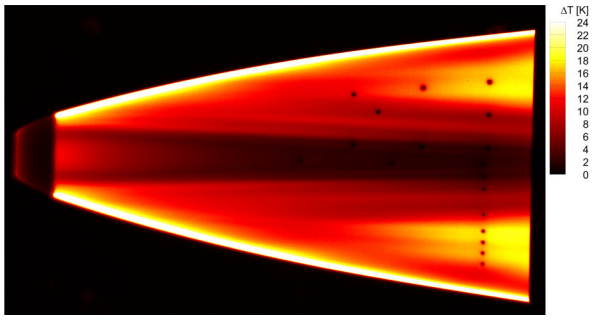

(d) run 7: $Ma_\infty = 5.986$, $\alpha = -2.20°$

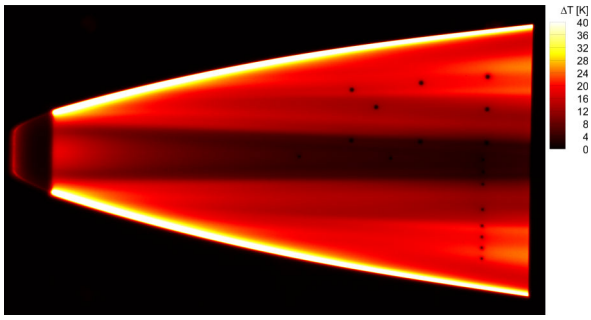

(e) run 33: $Ma_\infty = 7.013$, $\alpha = -2.00°$

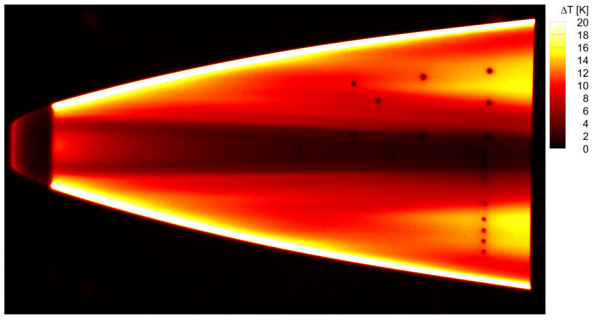

(f) run 36: $Ma_\infty = 5.986$, $\alpha = 0.00°$

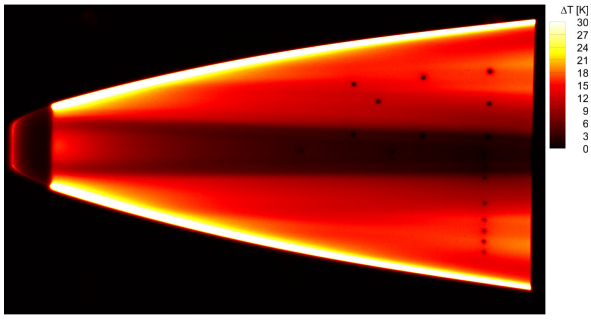

(g) run 23: $Ma_\infty = 7.013$, $\alpha = 0.00°$

Figure 3.20: Surface temperature increase for α from $-8°$ to $0°$

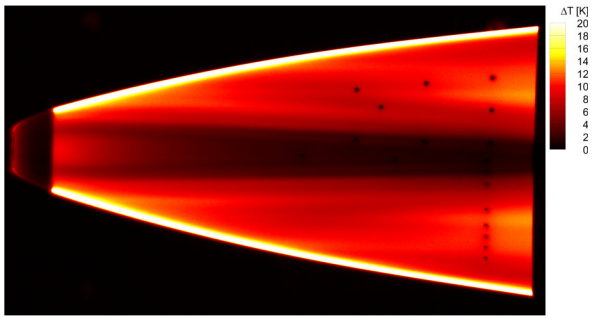

(a) run 6: $Ma_\infty = 5.987$, $\alpha = 1.80°$

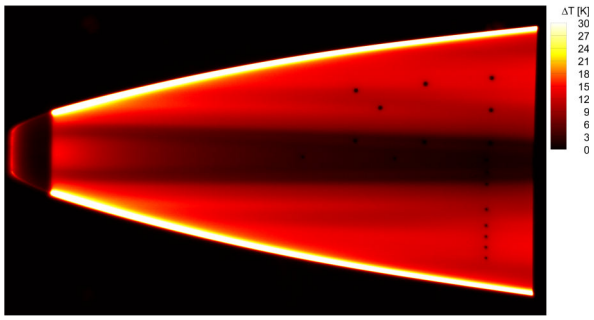

(b) run 32: $Ma_\infty = 7.013$, $\alpha = 2.00°$

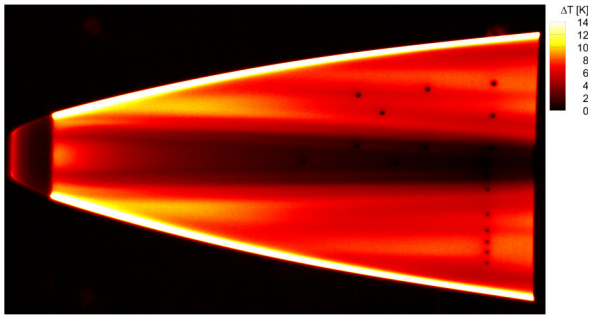

(c) run 9: $Ma_\infty = 5.985$, $\alpha = 3.80°$

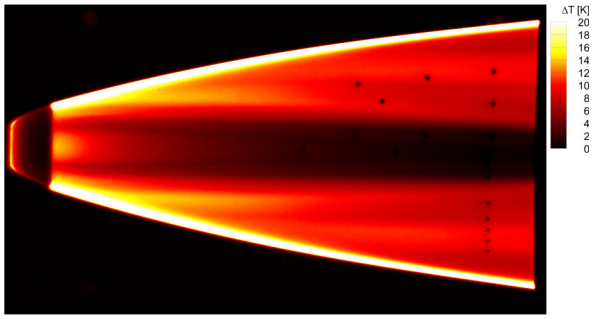

(d) run 26: $Ma_\infty = 7.012$, $\alpha = 4.00°$

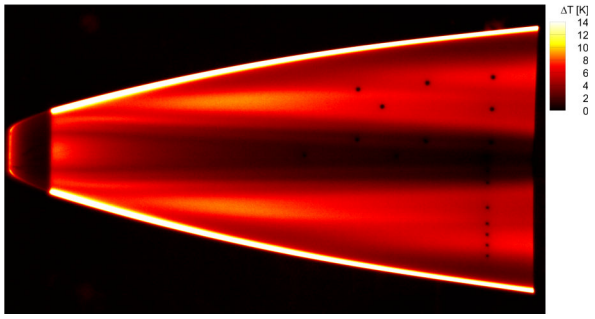

(e) run 37: $Ma_\infty = 5.986$, $\alpha = 6.00°$

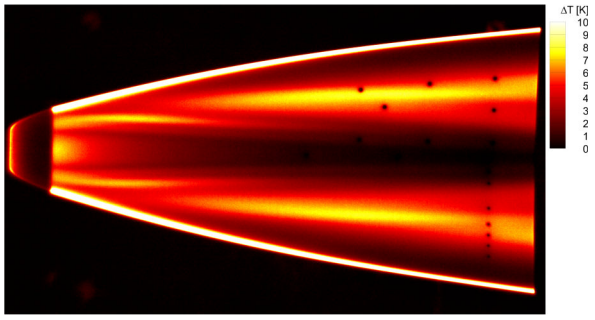

(f) run 10: $Ma_\infty = 5.987$, $\alpha = 7.80°$

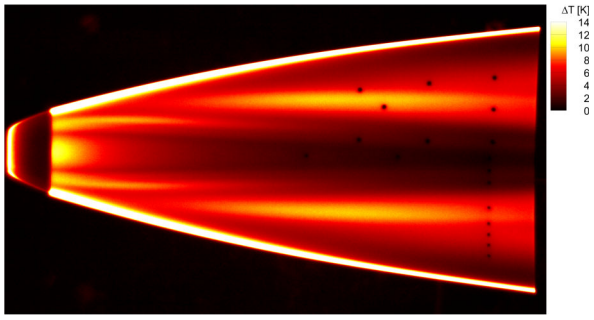

(g) run 34: $Ma_\infty = 7.013$, $\alpha = 8.00°$

Figure 3.21: Surface temperature increase for α from 2° to 8°

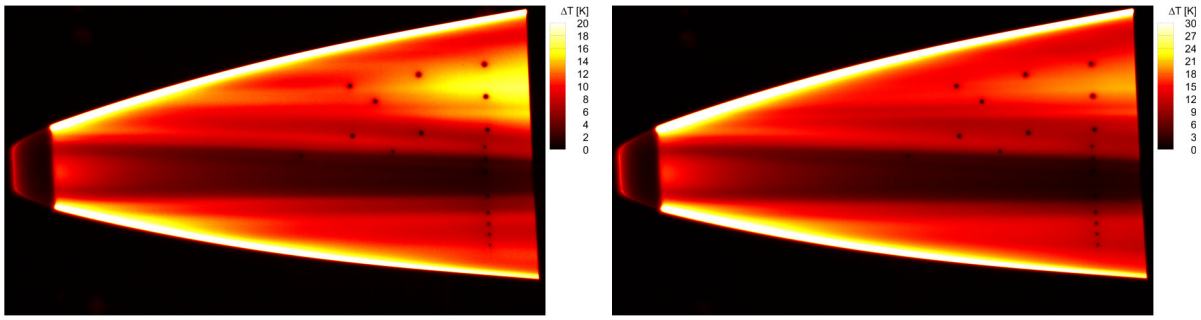

(a) run 15: $Ma_\infty = 5.986$, $\beta = -3.75°$ **(b)** run 29: $Ma_\infty = 7.012$, $\beta = -4.00°$

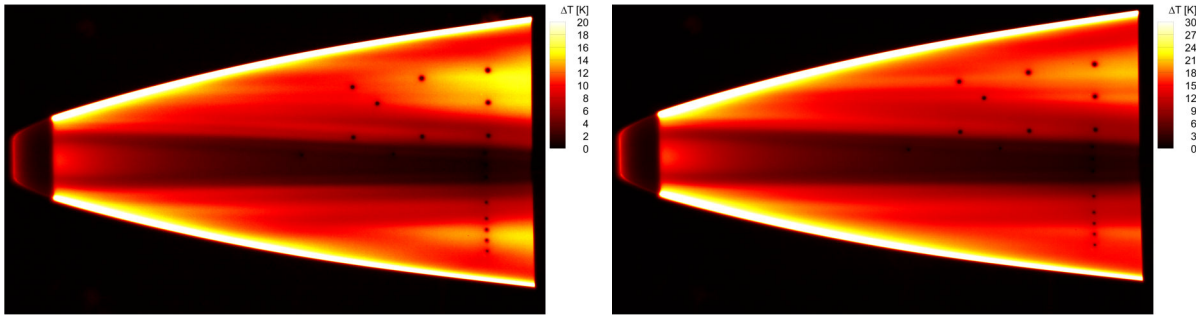

(c) run 14: $Ma_\infty = 5.986$, $\beta = -1.75°$ **(d)** run 30: $Ma_\infty = 7.014$, $\beta = -2.00°$

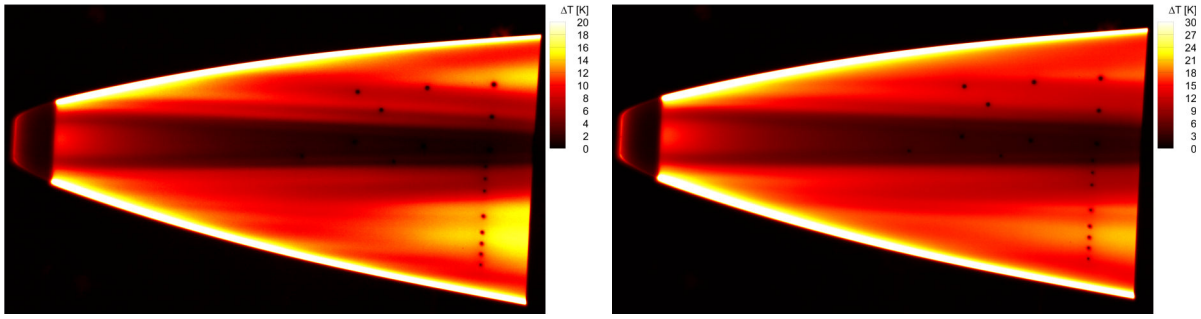

(e) run 12: $Ma_\infty = 5.987$, $\beta = 2.25°$ **(f)** run 31: $Ma_\infty = 7.013$, $\beta = 2.00°$

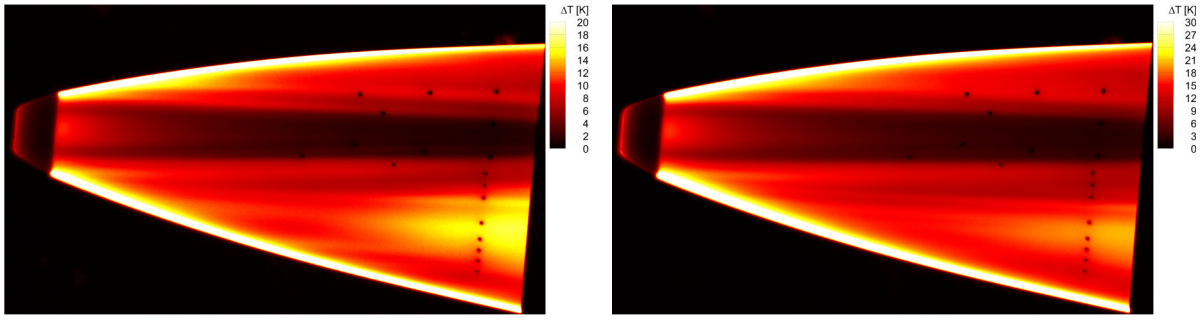

(g) run 13: $Ma_\infty = 5.987$, $\beta = 4.25°$ **(h)** run 28: $Ma_\infty = 7.013$, $\beta = 4.00°$

Figure 3.22: Surface temperature increase for β from $-4°$ to $4°$

3.3.4 Nose heating

Figure 3.23 shows the increase of the nose temperature for experiments at zero angle of attack and zero yaw angle. They are measured with TCK1 at $x = 21\,\text{mm}$ and TCK2 at $x = 3\,\text{mm}$. This reveals that the nose can become significant hot, which probably has to be taken into account when simulating the experiments.

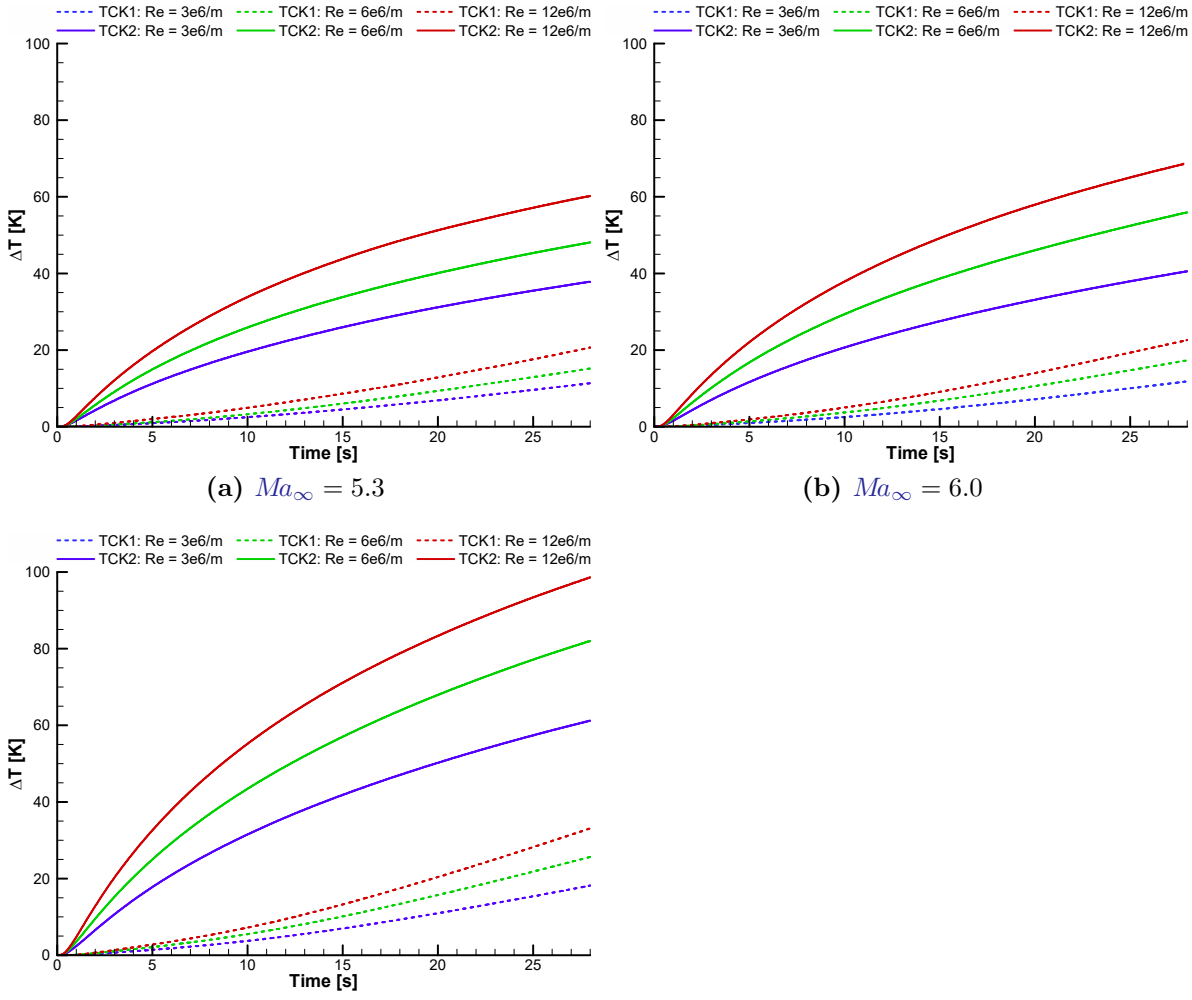

(a) $Ma_\infty = 5.3$ **(b)** $Ma_\infty = 6.0$

(c) $Ma_\infty = 7.0$

Figure 3.23: Increase of nose temperature

4 Conclusion

Within this report the experiments performed with the BOLT geometry in H2K at DLR are described. The acquired data are analysed in detail. Still to be done is the mapping of the IR data onto 3D surfaces and the computation of heat fluxes from the measured surface temperatures. Nevertheless the influence of Mach number, Reynolds number, angle of attack and yaw angle could be documented. Several interesting features including evidence for second (Mach) modes could be detected. It is planned to publish the findings in a journal paper.

5 Bibliography

[1] Berridge, D. C., G. McKiernan, T. P. Wadhams, M. Holden, B. M. Wheaton, T. D. Wolf, and S. P. Schneider, "Hypersonic Ground Tests In Support of the Boundary Layer Transition (BOLT) Flight Experiment", in *2018 Fluid Dynamics Conference*. DOI: 10.2514/6.2018-2893. eprint: https://arc.aiaa.org/doi/pdf/10.2514/6.2018-2893.

[2] Knutson, A. L., J. S. Thome, and G. V. Candler, "Numerical Simulation of Instabilities in the Boundary-Layer Transition Experiment Flowfield", *Journal of Spacecraft and Rockets*, vol. 58, no. 1, pp. 90–99, 2021. DOI: 10.2514/1.A34599. eprint: https://doi.org/10.2514/1.A34599.

[3] Kostak, H. E. and R. D. W. Bowersox, "Preflight Ground Test Analyses of the Boundary Layer Transition (BOLT) Flight Geometry", *Journal of Spacecraft and Rockets*, vol. 58, no. 1, pp. 67–77, 2021. DOI: 10.2514/1.A34858. eprint: https://doi.org/10.2514/1.A34858.

[4] Niezgodka, F.-J., *Der Hyperschallwindkanal H2K des DLR in Köln-Porz (Stand 2000)*, German, DLR-Mitteilungen. Köln: Deutsches Zentrum für Luft- und Raumfahrt e. V., 2001, p. 71. URL: http://elib.dlr.de/13874/.

[5] Wheaton, B. M., D. C. Berridge, T. D. Wolf, R. T. Stevens, and B. E. McGrath, "Boundary Layer Transition (BOLT) Flight Experiment Overview", in *2018 Fluid Dynamics Conference*. DOI: 10.2514/6.2018-2892. eprint: https://arc.aiaa.org/doi/pdf/10.2514/6.2018-2892.

A Appendix

A.1 Sensor Positions

name	type	x [mm]	y [mm]	z [mm]
PCB1	PCB	287.500	39.465	−55.000
PCB2	PCB	287.500	37.065	−13.750
PCB3	PCB	307.500	40.785	−41.250
PCB4	PCB	343.750	46.790	−61.250
PCB5	PCB	343.750	43.805	−13.750
PCB6	PCB	397.500	53.895	−66.875
PCB7	PCB	397.500	51.545	−40.625
PCB8	PCB	397.500	50.305	−13.750
KPT01	Kulite	245.000	31.755	0.000
KPT02	Kulite	320.000	40.795	0.000
KPT03	Kulite	395.000	49.840	0.000
KPT04	Kulite	395.000	49.930	10.000
KPT05	Kulite	395.000	50.185	20.000
KPT06	Kulite	395.000	51.235	40.500
KPT07	Kulite	395.000	52.255	53.500
KPT08	Kulite	395.000	53.125	62.500
KPT09	Kulite	395.000	54.090	71.250
KPT10	Kulite	395.000	55.185	80.000
PSI01	PSI	120.000	16.685	0.000
PSI02	PSI	380.000	51.850	−67.500
PSI03	PSI	380.000	48.030	0.000
PSI04	PSI	380.000	51.850	67.500
PSI05	PSI	120.000	−16.685	0.000
PSI06	PSI	380.000	−51.850	−67.500
PSI07	PSI	380.000	−48.030	0.000
PSI08	PSI	380.000	−51.850	67.500

name	type	x [mm]	y [mm]	z [mm]
PSI09	PSI	120.000	0.000	−51.460
PSI10	PSI	125.000	0.000	−52.300
PSI11	PSI	380.000	−30.000	−84.519
PSI12	PSI	380.000	0.000	−73.082
PSI13	PSI	380.000	30.000	−84.519
PSI14	PSI	120.000	0.000	51.460
PSI15	PSI	125.000	0.000	52.300
PSI16	PSI	380.000	−30.000	84.519
PSI17	PSI	380.000	0.000	73.082
PSI18	PSI	380.000	30.000	84.519
TCK1	thermocouple	21.000	0.000	−5.000
TCK2	thermocouple	3.000	0.000	5.000

A.2 Run Conditions

run	Ma_∞ [ ]	p_0 [kPa]	T_0 [K]	α [°]	β [°]	p_∞ [Pa]	T_∞ [K]	v_∞ $\left[\frac{\mathrm{m}}{\mathrm{s}}\right]$	$Re_{\mathrm{u},\infty}$ $\left[\frac{10^6}{\mathrm{m}}\right]$
1	6.025	869.767	496.524	-0.20	0.25	536.7	60.10	936.5	6.989
2	5.987	386.077	499.284	-0.20	0.25	247.7	61.12	938.3	3.126
3	5.986	379.836	505.042	-0.20	0.25	244.0	61.84	943.7	3.025
4	6.017	755.246	503.620	-0.20	0.25	470.3	61.12	943.0	5.963
5	6.054	1490.674	499.755	-0.20	0.25	893.9	60.00	940.0	11.725
6	5.987	376.829	495.054	1.80	0.25	241.9	60.61	934.3	3.091
7	5.986	373.309	497.618	-2.20	0.25	239.8	60.93	936.7	3.039
8	5.987	373.665	495.559	-4.20	0.25	240.0	60.67	934.8	3.061
9	5.985	379.824	511.920	3.80	0.25	244.2	62.70	950.1	2.965
10	5.987	373.699	493.078	7.80	0.25	239.9	60.36	932.5	3.084
11	5.987	376.667	494.617	-8.20	0.25	241.8	60.55	933.9	3.094
12	5.987	375.050	494.267	-0.20	2.25	240.8	60.51	933.6	3.084
13	5.987	372.980	493.403	-0.20	4.25	239.5	60.41	932.8	3.075
14	5.986	371.009	495.656	-0.20	-1.75	238.3	60.69	934.9	3.039
15	5.986	372.413	503.743	-0.20	-3.75	239.4	61.69	942.5	2.978
16	5.987	372.960	494.312	1.80	2.25	239.5	60.52	933.6	3.067
17	5.986	369.897	492.711	-0.20	0.25	237.6	60.33	932.1	3.057
18	5.276	252.769	469.756	-0.20	0.25	348.3	71.53	894.5	3.059

run	Ma_∞ [ ]	p_0 [kPa]	T_0 [K]	α [°]	β [°]	p_∞ [Pa]	T_∞ [K]	v_∞ $\left[\frac{\mathrm{m}}{\mathrm{s}}\right]$	$Re_{\mathrm{u},\infty}$ $\left[\frac{10^6}{\mathrm{m}}\right]$
19	5.298	506.414	469.656	-0.20	0.25	681.0	71.02	895.0	6.070
20	5.317	1004.226	469.290	-0.20	0.25	1320.9	70.52	895.1	11.944
21	7.012	711.624	581.720	-0.05	0.00	170.0	53.69	1030.1	3.051
22	7.012	726.242	591.167	0.05	0.00	173.5	54.56	1038.4	3.040
23	7.013	732.068	589.540	0.00	0.00	174.8	54.41	1037.0	3.076
24	7.047	1451.945	596.743	0.00	0.00	336.2	54.59	1043.7	5.915
25	7.104	2934.662	583.443	0.00	0.00	645.5	52.60	1032.8	12.106
26	7.012	724.547	591.398	4.00	0.00	173.1	54.59	1038.6	3.031
27	7.013	736.891	588.385	-4.00	0.00	175.9	54.29	1036.0	3.105
28	7.013	728.255	589.568	0.00	4.00	173.9	54.41	1037.0	3.060
29	7.012	727.981	590.943	0.00	-4.00	173.9	54.54	1038.2	3.048
30	7.014	736.014	579.952	0.00	-2.00	175.6	53.51	1028.5	3.168
31	7.013	734.157	586.930	0.00	2.00	175.2	54.16	1034.7	3.105
32	7.013	727.143	587.890	2.00	0.00	173.6	54.26	1035.5	3.068
33	7.013	736.658	594.042	-2.00	0.00	175.9	54.82	1040.9	3.060
34	7.013	728.575	582.255	8.00	0.00	173.9	53.73	1030.5	3.118
35	5.987	371.523	493.015	-0.06	-0.03	238.6	60.36	932.4	3.067
36	5.986	367.264	497.203	0.00	-0.03	236.0	60.89	936.3	2.995
37	5.986	370.118	493.804	6.00	0.00	237.7	60.46	933.1	3.048